



Australian Government
Bureau of Meteorology

The Centre for Australian Weather and Climate Research
A partnership between CSIRO and the Bureau of Meteorology



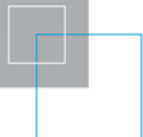
CAWCR Research Letters

Issue 4, July 2010

P.A. Sandery, T. Leeuwenburg, G. Wang, A.J. Hollis, K.A. Day (editors)



www.cawcr.gov.au



ISSN: 1836-5949

Series: Research Letters (The Centre for Australian Weather and Climate Research); Issue 4.

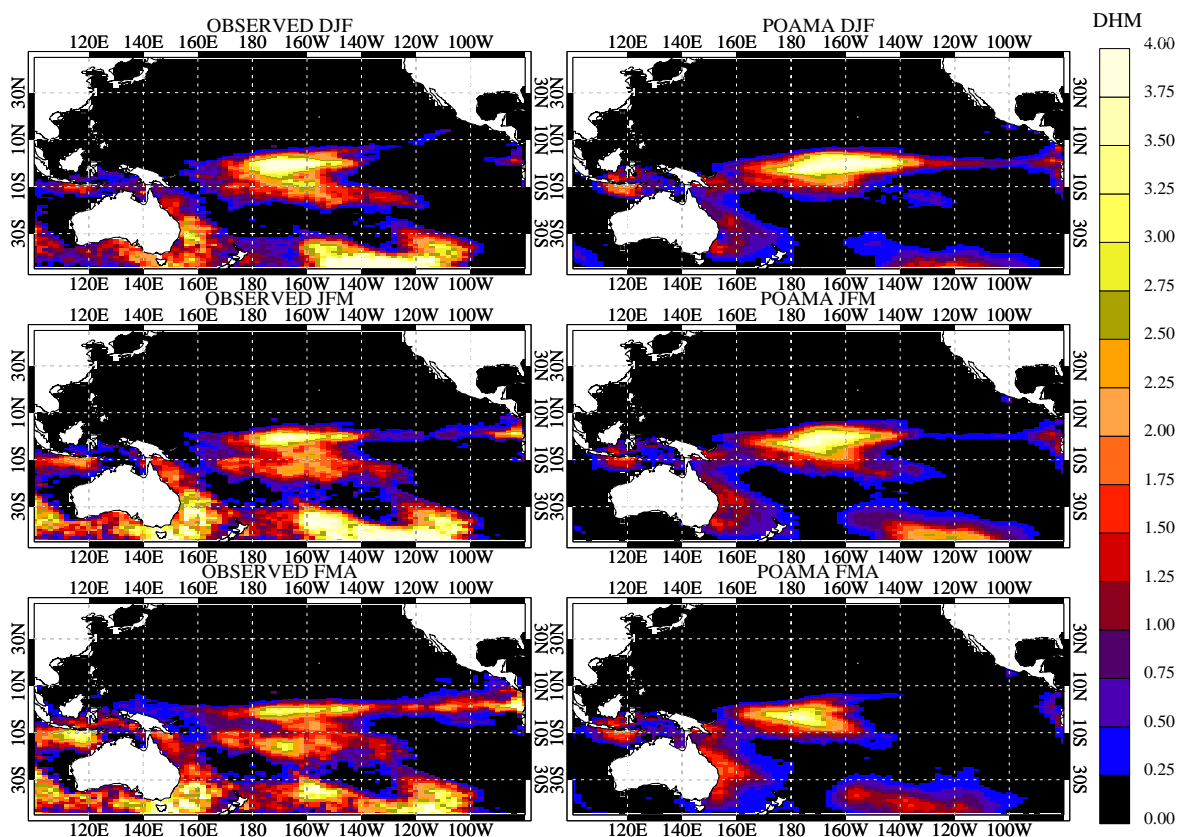
Copyright and Disclaimer

© 2010 CSIRO and the Bureau of Meteorology. To the extent permitted by law, all rights are reserved and no part of this publication covered by copyright may be reproduced or copied in any form or by any means except with the written permission of CSIRO and the Bureau of Meteorology.

CSIRO and the Bureau of Meteorology advise that the information contained in this publication comprises general statements based on scientific research. The reader is advised and needs to be aware that such information may be incomplete or unable to be used in any specific situation. No reliance or actions must therefore be made on that information without seeking prior expert professional, scientific and technical advice. To the extent permitted by law, CSIRO and the Bureau of Meteorology (including each of its employees and consultants) excludes all liability to any person for any consequences, including but not limited to all losses, damages, costs, expenses and any other compensation, arising directly or indirectly from using this publication (in part or in whole) and any information or material contained in it.

Contents

Evaluation of low latitude cloud properties in ACCESS and HadGEM AMIP simulations	C. Franklin and M. Dix	4
Real-time seasonal SST predictions for the Great Barrier Reef during the summer of 2009/2010	C. Spillman, D. Hudson and O. Alves	11
A discussion on aspects of the seasonality of the rainfall decline in South-Eastern Australia	B. Timbal	20
Evaluation of ACCESS-A Clouds and Convection using Near Real-Time CloudSat-CALIPSO Observations	A. Protat, L. Rikus, S. Young, J. Le Marshall, P. May, and M. Whippey	27



Editors: P.A. Sandery, T. Leeuwenburg, G. Wang, A.J. Hollis, K.A. Day
Enquiries: Dr Paul Sandery p.sandery@bom.gov.au
 CAWCR Research Letters
 The Centre for Australian Weather and Climate Research
 Bureau of Meteorology
 GPO Box 1298 Melbourne VICTORIA 3001

CAWCR Research Letters is an internal serial online publication aimed at communication of research carried out by CAWCR staff and their colleagues. It follows on from its predecessor *BMRC Research Letters*. Articles in *CAWCR Research Letters* are peer reviewed and typically 4-8 pages in length. For more information visit the CAWCR website.

Evaluation of low latitude cloud properties in ACCESS and HadGEM AMIP simulations

Charmaine Franklin and Martin Dix

Centre for Australian Weather and Climate Research,

CSIRO Marine and Atmospheric Research

charmaine.franklin@csiro.au

Introduction

The radiative impact of clouds is an important aspect of the tropical circulation. Cloud forcing influences surface heating gradients, and consequently can impact large-scale circulations and ocean heat transports. An accurate representation of the radiative effect of clouds is therefore imperative to correctly simulate feedbacks in a coupled ocean-atmosphere model. Differences in cloud behaviour between models are the dominant source of uncertainty in the prediction of overall climate sensitivity (e.g. Colman 2003). As climate models are a key tool used to predict future climate change, greater confidence in climate projections requires better understanding and representation of clouds and their feedbacks in these models.

The cloud radiative effect from simulations can be examined by defining dynamically based cloud regimes according to midtropospheric vertical velocity. In the tropics this covers the deep convective through to the strongly subsiding regimes that span the range of cloud distributions associated with the overturning circulation. In this study we use the compositing method of Bony et al. (2004), as described in Franklin and Dix (2009), to examine the radiative impact of low latitude clouds from four AMIP simulations. Relationships between tropical cloud properties and convective precipitation are also examined to identify model biases and aid model development. These relationships characterise the coupling between the column radiation budget and the hydrological cycle commonly described by the concept of radiative-convective equilibrium: atmospheric radiative cooling is balanced energetically by the transport of surface latent and sensible heat by the process of convection. This

work extends that presented in Franklin and Dix (2009) and adds to the efforts underway in examining possible atmospheric model configurations to be used in ACCESS.

Model description

Four AMIP simulations will be examined in this study. One is the ACCESS simulation that was analysed in Franklin and Dix (2009) and is based on HadGEM1 with bug fixes and the addition of an early version of the PC2 (prognostic cloud, prognostic condensate) cloud scheme (Wilson et al. 2008a). In the following discussions this simulation will be referred to as HadGEM1 for brevity, however, it needs to be emphasised that the model configuration is distinctly different to that of HadGEM1, particularly through the use of PC2. The other three simulations are HadGEM2 (using the configuration documented in Collins et al. 2008) and prototype HadGEM3 AMIP simulations, all performed by the Hadley Centre. More details of the ACCESS and two of the Hadley Centre simulations are given in Rashid et al. (2009). The additional simulation uses a prototype HadGEM3 configuration with 63 vertical levels rather than the 38 levels used in all of the other simulations. HadGEM3 is currently being developed at the UK Met Office and the version used in this work is that used in the March 2009 assessment report from the Hadley Centre.

A description of the physical parameterisations used in the Unified Model and their references are given in Franklin and Dix (2009). A detailed description of the differences between the parameterisations used in the simulations analysed in this study is beyond the scope of this short paper. Some of the key differences pertinent to the results presented herein are: all simulations except

HadGEM2 use the PC2 cloud scheme, while HadGEM2 uses the Smith cloud scheme (Smith 1990) with modifications (Wilson et al. 2007) and a diagnostic convective cloud fraction (Gregory 1999); the convection scheme includes an adaptive detrainment parameterisation in the HadGEM2 and prototype HadGEM3 simulations, and; the prototype HadGEM3 simulations use a vertical velocity CAPE closure rather than a relative humidity based CAPE closure, a new scalar flux-gradient formulation in the boundary layer and numerous modifications to remove level dependencies in parameterisations, particularly the convection scheme.

Regime based evaluation of low latitude cloud properties

To evaluate the regime based cloud properties from the AMIP simulations, the tropical circulation (30°N–30°S) is decomposed following Bony et al. (2004) using the pressure velocity at 500 hPa as a proxy for the large-scale circulation. Cloud and radiative properties are composited as a function of the circulation regime, covering deep convective clouds through to boundary layer clouds associated with the subsidence of the overturning circulation. The shortwave and longwave cloud radiative forcing (CRF_{SW} , CRF_{LW}) are calculated as the difference between the clear-sky and all-sky radiation to infer how the clouds affect the radiation budget at the top of the atmosphere. The validation data used to evaluate the models are documented in Franklin and Dix (2009). The model output and validation data have been interpolated onto the same grid (2.8° x 2.8°) and monthly climatologies have been used in the following analysis.

Figure 1 shows the CRF_{SW} , CRF_{LW} and total cloud forcing as a function of circulation regime. The ERBE observations have been composited as a function of the pressure velocity from both the ERA15 and NECP reanalyses to give an indication of the uncertainty associated with the vertical motion. For the convective regimes of the tropics all simulations underestimate the strength of the observed CRF_{SW} , with HadGEM3-38 producing values closest to the observations. The clouds produced by the models in the subsidence regimes with vertical motion between about 20 and 40 hPa day⁻¹ are also not reflecting enough shortwave radiation, predominately due to the

significant underestimate of cloud cover (see Fig. 2).

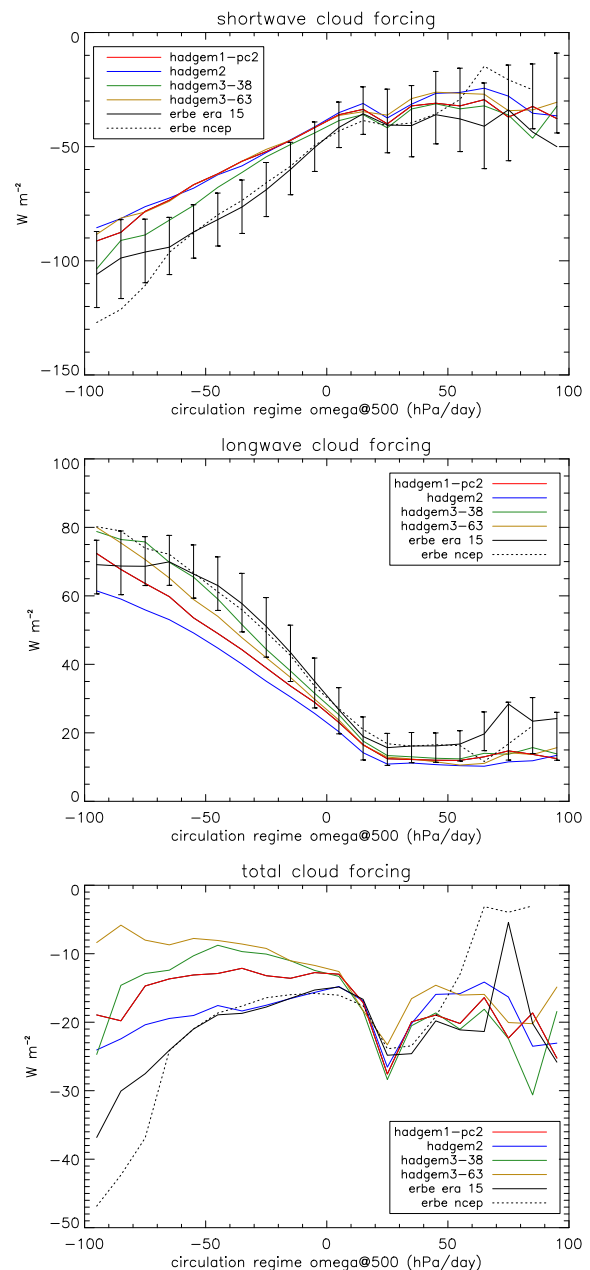


Fig. 1 Shortwave, longwave and total cloud radiative forcing as a function of circulation regime. The bars represent the 25th and 75th percentiles of the ERBE observations when composited as a function of the ERA15 pressure velocity.

On average the CRF_{SW} from the models is underestimated by about 20 W m⁻², though we note that there is a large range of variability associated with the weakly convective and all subsidence regimes. Given

that the errors for the sensors used in ERBE are about 10 W m^{-2} (Barkstrom 1984) and that a bias due to clear-sky fluxes in the ERBE CRF_{sw} is an underestimate of $5\text{-}10 \text{ W m}^{-2}$ (Stubenrauch et al. 2002), this reinforces the systematic bias in the models to not produce strong enough CRF_{sw} for tropical convective regimes. The CRF_{LW} from the simulations generally has a smaller bias than the CRF_{sw} , except for the HadGEM2 simulation where the biases are about the same magnitude in both components. The HadGEM2 model is the only model considered in this study that uses the Smith cloud scheme. The other simulations use PC2, which produces larger cloud fractions as shown in Fig. 2 and Table 1.

Table 1: Total cloud cover (%) global root mean squared error and bias as measured from ISCCP. The first row indicates the model simulation; see the previous section for model descriptions.

	1-PC2	2	3-38	3-63
RMSE	13.8	15.5	13.4	13.0
bias	-2.2	-12.4	0.1	-1.2

Note that the cloud fractions are the total cloud fractions and, therefore, include contributions from the diagnostic convective cloud fraction used in HadGEM2 along with the Smith scheme. The larger cloud fractions produced by PC2 are in better agreement with observations and the global average bias is ten percent lower compared to the result from the Smith scheme plus the diagnostic convective cloud fraction (see Table 1). PC2 also produces deeper clouds than those produced by the Smith scheme (Wilson et al. 2008b). The deeper and more extensive clouds in the simulations using PC2 absorb longwave radiation and reradiate to space at the colder cloud top temperatures, thus producing stronger CRF_{LW} in the HadGEM1 and HadGEM3 simulations. This stronger CRF_{LW} is in better agreement with the observations compared to the HadGEM2 result, though still not strong enough.

Combining the components of cloud forcing shows that a cancellation of errors produces a good representation of the total cloud forcing from HadGEM2 throughout most of the convective regimes, except for those associated with upward motion exceeding -50 hPa day^{-1} (see Fig. 1). Even for these strongly convective regimes though, the total cloud forcing from HadGEM2 is in better agreement with the ERBE

observations than those from the other AMIP simulations. The total cloud forcing of the subsidence cloud regimes is better simulated with HadGEM1 and HadGEM3-38, which is due to the individual shortwave and longwave components being more representative of the observations for these simulations.

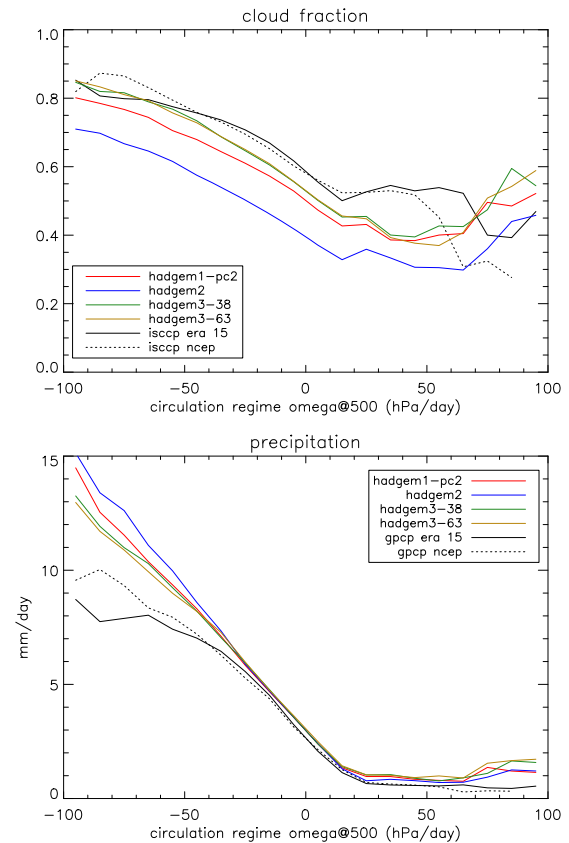


Fig. 2 Total cloud fraction and precipitation as a function of circulation regime.

The HadGEM3 results for the convective regimes between 0 and -50 hPa day^{-1} show that the total cloud forcing in Fig. 1 weakens towards zero as the convective precipitation increases (see Fig. 2). This is opposite to the observations and the HadGEM2 simulation that show a decrease and, therefore, an intensification of the total cloud forcing. This error is predominately due to the underestimate of the CRF_{sw} and the inability of the model to produce the observed increase in cloud fraction and optical depth for increasing convective precipitation rates. The increase towards zero in total cloud forcing implies that HadGEM3 is trapping more radiant energy as

convection increases throughout this range of regimes. The trapping of radiant energy continues into the deep convective regimes for HadGEM3-63,

however, HadGEM3-38 converges towards the observed total cloud forcing as the precipitation rate exceeds 10 mm day⁻¹.

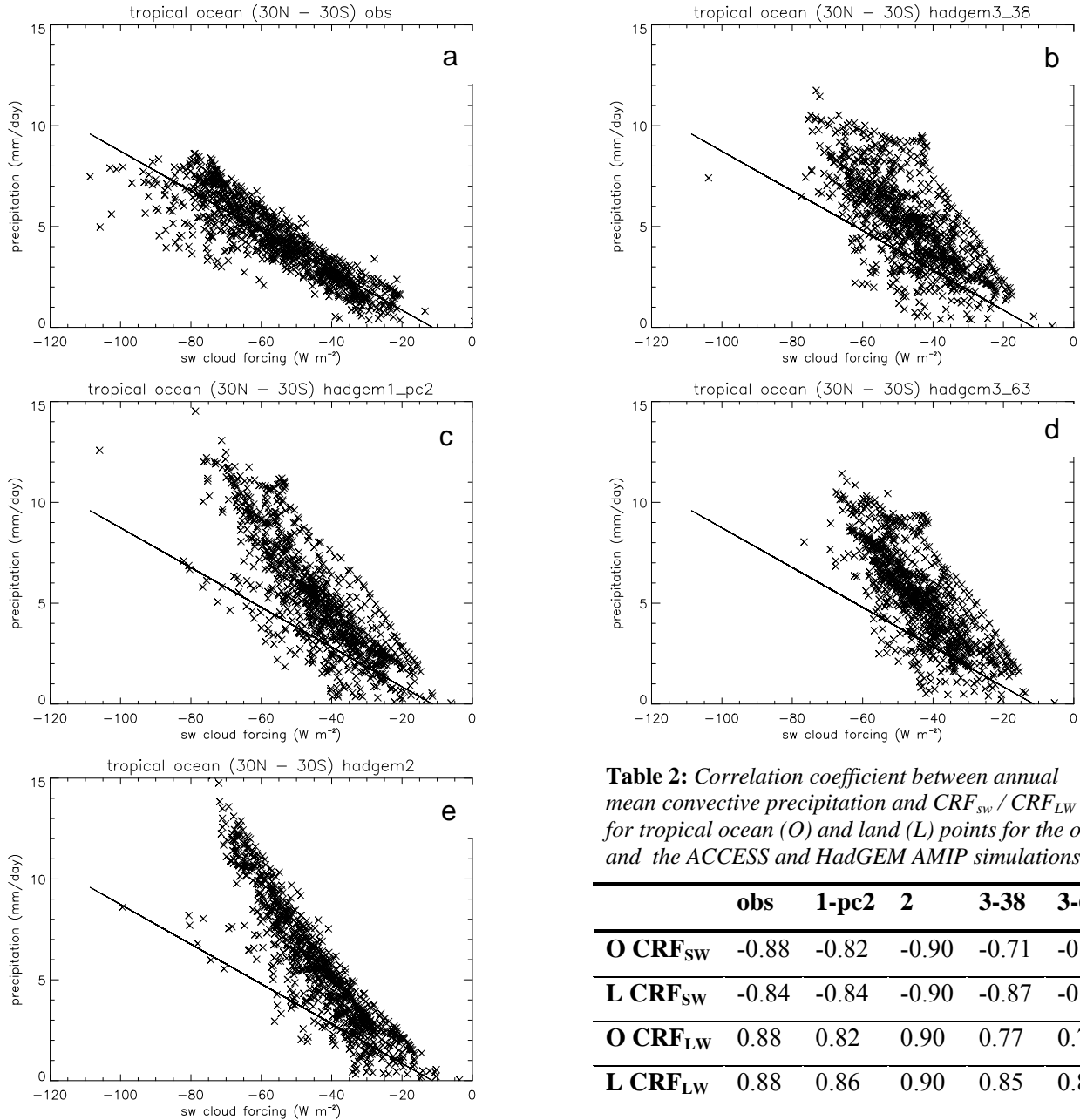


Table 2: Correlation coefficient between annual mean convective precipitation and CRF_{SW} / CRF_{LW} for tropical ocean (O) and land (L) points for the obs and the ACCESS and HadGEM AMIP simulations.

	obs	1-pc2	2	3-38	3-63
O CRF_{SW}	-0.88	-0.82	-0.90	-0.71	-0.77
L CRF_{SW}	-0.84	-0.84	-0.90	-0.87	-0.87
O CRF_{LW}	0.88	0.82	0.90	0.77	0.79
L CRF_{LW}	0.88	0.86	0.90	0.85	0.85

Fig. 3 Convective precipitation versus CRF_{SW} over the tropical oceans ($30^{\circ}N-30^{\circ}S$) with annual mean SST > 27°C for a) the ERBE and GPCP observations, b) HadGEM1-PC2, c) HadGEM2, d) HadGEM3 – 38 levels and e) HadGEM3 – 63 levels. The line shown in each panel is the best-fit linear regression line to the observed relationship.

Relationships between tropical precipitation and cloud forcing

The relationship between convective precipitation and

CRF_{SW} over the tropical oceans is shown in Fig. 3. Each point represents annual mean values for grid boxes that are between $30^{\circ}N$ and $30^{\circ}S$

and where the annual mean SST exceeds 27°C. The observations show a strong linear relationship with a correlation coefficient of -0.88 (see Table 2): the CRF_{SW} decreases as the observed convective precipitation increases due to greater reflection of solar radiation.

The HadGEM2 results show a slightly stronger association between CRF_{SW} and convective precipitation than the observations with a correlation coefficient of -0.9. While this correlation coefficient is in better agreement with the observations than the other simulations, the bias for high precipitation rates is the largest for HadGEM2 resulting in the poorest regression

coefficient (see Fig. 4a). HadGEM2 is the only model examined in this study to exhibit a stronger association than the observations between precipitation and cloud forcing, and this is also the only model to use the Smith cloud scheme. One of the motivations behind the development of PC2 was to enable more variability in cloud properties and this result can be seen in the scatter plots of Fig. 3. As shown in Figs. 2, 3d and 3e the changes that have been made to the convection scheme in HadGEM3 result in a better representation of convective precipitation in the tropics, however, the annual mean for most of the tropical cloud regimes still exceeds that observed (Fig. 2).

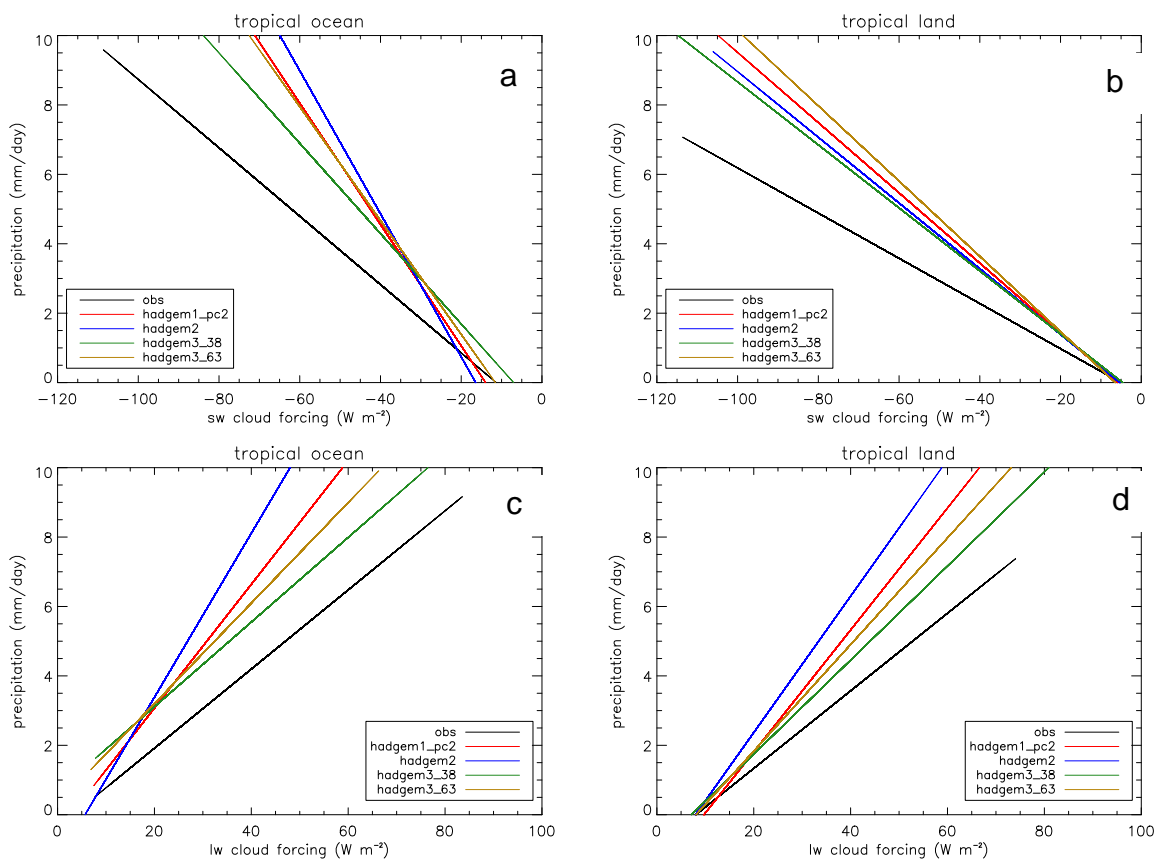


Fig. 4 a) Observed and modelled relationships between convective precipitation and SW cloud forcing over the tropical oceans found by linear regression. b) as for a) except for the tropical land points, c) as for a) except for the LW cloud forcing and d) as for c) except for the tropical land points.

Figure 4a shows the results of linear regression of convective precipitation against CRF_{SW} for the observations and the four AMIP simulations that were presented in Fig. 3. From this figure it is

clear that the HadGEM3-38 results produce the closest relationship to that observed. The results of the same analysis technique are shown in Fig. 4b, however, this is for tropical land points

rather than oceanic. Over land the models and observations show a reduced slope compared to that for oceanic convection, this reflects the higher reflectivity of convective clouds over land. There is reasonable agreement between the observed and modelled CRF_{SW} over tropical land points for low precipitation rates of 1 mm day^{-1} , however, the models diverge away from the observed relationship as the strength of the precipitation increases. The HadGEM2 simulation produces an improved relationship between convective precipitation and CRF_{SW} over land than over the ocean. This is due to the reduced bias in precipitation produced by this model over tropical land points.

Figures 4c and 4d show the regression results for CRF_{LW} against convective precipitation over tropical ocean and land points, respectively. The slope of the HadGEM-38 oceanic results closely resembles that from the observations, with a bias of about -10 Wm^{-2} constant across all precipitation rates. Similarly to the CRF_{SW} results over the ocean in Fig. 4a, the CRF_{LW} relationship with convective precipitation from HadGEM2 is the least representative to the observed relationship and this is also the case for the CRF_{LW} over land. This is in agreement with the results presented in the previous section and is due to the greater cloud fractions and deeper clouds produced by the other simulations that all use PC2, which results in stronger cloud forcing that more closely resembles the observations.

Conclusions

The total cloud radiative forcing from the HadGEM2 AMIP simulation was shown to produce the most accurate representation for tropical cloud regimes composited as a function of midtropospheric velocity. However, this result is due to the cancellation of errors between the CRF_{SW} and CRF_{LW} . The prototype HadGEM3 simulation with 38 vertical levels simulates stronger cloud radiative forcing in both components and as such agrees more with the ERBE observations than the other AMIP simulations. However, even from this simulation the cloud radiative forcing is too weak and this has been shown to be a systematic bias in the models examined in this study. The two prototype HadGEM3 simulations show that for the convective regimes with 500 hPa vertical

velocities between 0 and -50 hPa day^{-1} , the total cloud forcing increases with increasing convective precipitation. This implies that the model is trapping radiant energy as the convection intensifies throughout these regimes and is opposite to the observations that show total cloud forcing decreasing across these regimes. This error is predominately due to the underestimate of the CRF_{SW} and the inability of the model to produce the observed increase in cloud fraction and optical depth for increasing convective precipitation rates.

The relationship between tropical cloud properties and convective precipitation has been examined and systematic biases have been found. None of the model results examined in this study produced strong enough radiative cloud forcing for a given amount of convective precipitation. While the models were able to correctly differentiate between the relationships over tropical land and ocean, there is a general tendency for the bias in the cloud forcing to increase as the convective precipitation increases. For example, the CRF_{SW} bias over the tropical ocean from the prototype HadGEM3-38 simulation increases from 7 Wm^{-2} for a convective precipitation rate of 1 mm day^{-1} to approximately 23 Wm^{-2} for an 8 mm day^{-1} precipitation rate. The underestimate of the CRF_{SW} may contribute to errors in the model precipitation and its response to warming. This may have implications for cloud feedbacks and changes to the intensity of the global hydrological cycle in perturbed climate simulations.

Acknowledgements

Thanks to Dr Gill Martin from the UK Met Office Hadley Centre for providing model output from the HadGEM2 and HadGEM3-38 and HadGEM3-63 AMIP simulations and for providing helpful comments on this note. Thanks to Zhian Sun and Harun Rashid for their reviews and feedback.

References

- Barkstrom, B.R. 1984. The Earth Radiation Budget Experiment (ERBE). *Bull. Amer. Meteor. Soc.*, **65**, 2493-525.
- Bony, S. and co-authors. 2004. On dynamic and thermodynamic components of cloud changes. *Climate Dyn.*, **22**, 71-86.
- Collins, W., Bellouin, N., Doutriaux-Boucher, M., Hinton, T., Jones, C.D., Fiddicoat, S., Martin, G., O'Connor, F., Rae, J., Reddy, S., Senior, C., Totterdell, I. and Woodard, S.

2008. *Evaluation of the HadGEM2-ES model*. Hadley Centre Technical Note 74, 43pp. Available online at <http://www.metoffice.gov.uk/research/hadleycentre/pubs/HCTN/index.html>
- Colman, R. 2003. A comparison of climate feedbacks in general circulation models. *Climate Dyn.*, **20**, 865-73.
- Franklin, C.N. and Dix, M. 2009. Analysis of low-latitude cloud properties in the ACCESS AMIP simulation – regime sorting using mid-tropospheric velocity. *CAWCR Research Letters*, **2**, 12-17.
- Gregory, J. 1999. Representation of the radiative effects of convective anvils. Hadley Centre Tech. Note 7. Met. Office, Exeter, UK.
- Rashid, H.A., Dix M. and Hirst, A.C. 2009. Surface energy balance in the ACCESS models: comparisons with observation based flux products. *CAWCR Research Letters*, **3**, 35-43.
- Stubenrauch, C.J., Briand, V. and Rossow, W.B. 2002. The role of clear-sky identification in the study of cloud radiative effects: Combined analysis from ISCCP and the scanner of radiation budget. *J. Appl. Meteor.*, **41**, 396-412.
- Smith, R.N.B. 1990. A scheme for predicting layer clouds and their water contents in a general circulation model. *Q. J. R. Meteorol. Soc.*, **116**, 435-60.
- Wilson, D.R., Smith, R.N.B., Gregory, D., Wilson, C.A., Bushell, A.C. and Cusack, S. 2007. The large-scale cloud scheme and saturated specific humidity. Unified Model documentation paper 26. Met. Office, Exeter, UK
- Wilson, D. and co-authors, 2008a. PC2: A prognostic cloud fraction and condensation scheme. I: Scheme description. *Q. J. R. Meteorol. Soc.*, **134**, 2093-107.
- Wilson, D. and co-authors, 2008b. PC2: A prognostic cloud fraction and condensation scheme. II: Climate model simulations. *Q. J. R. Meteorol. Soc.*, **134**, 2109-25.

Real-time seasonal SST predictions for the Great Barrier Reef during the summer of 2009/2010

C. M. Spillman, D. A. Hudson and O. Alves

Centre for Australian Weather and Climate Research

c.spillman@bom.gov.au

Introduction

Coral bleaching has been observed sporadically in the Great Barrier Reef, Australia, since 1982 (Done et al. 2003). Anomalously high ocean temperatures are recognised as the primary cause of mass coral bleaching events (Hoegh-Guldberg 1999), which are predicted to increase in both frequency and severity under global warming (Donner et al. 2005). The probable increase in the frequency of bleaching events highlights the importance of gaining insight into the processes of coral bleaching and developing appropriate management plans to minimise damage to the reef ecosystem during such events. Advance warning of potential bleaching events allows for the implementation of these plans to reduce reef damage and maximise the potential for recovery (Marshall and Schuttenberg 2006). Predictions on a seasonal time-scale are the most practical for reef managers, as strategies can be implemented at the start of summer prior to the onset of bleaching. Until recently, predictions of coral bleaching risk have been predominantly based on satellite-derived now-casts (e.g. McClanahan et al. 2007) or projections on climate change timescales (e.g. Donner et al. 2005).

New operational seasonal forecast products developed at the Australian Bureau of Meteorology, in collaboration with the Great Barrier Reef Marine Park Authority, aim to address this deficit in reef forecast tools (Spillman and Alves 2009). Operational seasonal forecasts of SST anomalies in the Great Barrier Reef (GBR) region are generated in real time using the Predictive Ocean Atmosphere Model for Australia (POAMA). POAMA is a coupled global ocean-atmosphere model and data assimilation ensemble forecast system, developed by the Bureau of Meteorology and CSIRO. In the real-time system, a nine month forecast is produced each day, with

the outlooks provided by POAMA based on an ensemble of the 30 most recent daily forecasts. The variability of the results among the forecasts (i.e. ensemble members) gives an indication of the uncertainty in the future evolution of the climate system and provides information as to the probability distribution of future conditions. Forecast products are hosted by Ocean Services at the Bureau of Meteorology (Spillman et al. 2009a) and updated daily online for reef managers at <http://www.bom.gov.au/oceanography>. For more details of the model setup and forecast generation see Spillman and Alves (2009) and Spillman et al. (2009b).

These forecasts form an important component of the GBRMPA Coral Bleaching Response Plan and reef management plans (Maynard et al. 2009). This paper gives an overview of sea surface temperatures (SST) in the GBR region for the summer of 2009/2010 and the skill of POAMA in predicting these conditions in real-time.

Observed summer conditions

Initial observations in the GBR region suggested that the summer of 2009/2010 would be a relatively average year. Observed satellite monthly SST anomalies from the Reynolds OI.v2 1° analysis showed cool conditions in November, with a large area of the region up to 0.3-0.4°C cooler than the long term SST mean for the month (Fig. 1). Some warming was evident in the southern GBR along the coast in December and January, though average SST conditions throughout the rest of the region were similar to long-term climatological values. Anomalies in February were generally higher than in January with a positive anomaly of 0.2-0.3°C over most of the region. In March and April, strong positive anomalies occurred in the northern GBR that were up to 1°C warmer than average (Fig. 1).

Widespread warming of SST in the Maritime Continent region was also observed in March and was largely due to the lack of intraseasonal weather activity in this area during this period¹.

The timing of the onset of the Australian monsoon and development of its bursts and breaks is often influenced by the Madden Julian Oscillation (MJO). The MJO is a global-scale feature of the tropical atmosphere and is associated with weekly to monthly periods of alternating active and inactive rainfall over parts of Australia and is generally most well developed in summer. Active periods bring broad areas of persistent rain, while break periods are generally drier, and often hotter, with only isolated thunderstorms and rain systems (e.g. Wheeler et al. 2009). During the summer of 2009/2010, an active MJO signal appeared in late December 2009 in the Indian Ocean and moved towards the western Pacific where it remained active throughout the end of January and most of February¹. Two tropical cyclones (TC) in January, TC Neville and TC Olga, combined with an active monsoon trough, resulted in heavy rainfall and flooding along the northeast tropical coast (Bureau of Meteorology 2010b). Another weak MJO signal appeared in the western Indian Ocean during mid February and propagated east through Australian longitudes.

A moderate El Niño event occurred during the summer of 2009/2010. Coral bleaching has occurred in tropical locations that have been shown to be correlated with ENSO indices (Goreau and Hayes 1994; Hoegh-Guldberg 1999; Goreau and Hayes 2005). Mass bleaching events often occur during strong El Niño periods, due to sustained regional elevations of ocean temperature (Hoegh-Guldberg 1999; Baker et al. 2008). NINO3.4 is an index used to describe ENSO and is defined as the areal average of monthly SST anomalies in the tropical Pacific Ocean (5 S–5 N, 170–120 W). Monthly NINO3.4 values were +1.8°C in December, +1.5°C in January, +1.2°C in February and +1.1°C in March. Incidentally the December value was the warmest monthly value since the El Niño of 1997/98 (Bureau of

Meteorology 2010a). Of the coral bleaching reports collected over the summer of 2009/2010 by Bleachwatch, a community based coral reef monitoring initiative by the Great Barrier Reef Marine Park Authority, only fifteen percent reported minor seasonal bleaching and two percent showed moderate bleaching. The moderate bleaching was mostly confined to shallow reef areas and the minor bleaching was uneven across affected coral colonies, suggesting the likely causes were probably exposure and rainfall resulting from the king tides in late January/February 2010, rather than temperature stress².

POAMA Summer Outlook

Forecasts issued in December...

The POAMA outlook for the summer of 2009/2010 in the GBR region was for an average summer season with only small SST anomalies evident during December-February, the warmest months of the year, indicating a low probability of conditions conducive to coral bleaching occurring. The real-time forecasts for the coming summer months, generated in December 2009, suggested minimal warming over the GBR region with SST anomalies around or below 0°C in December and January (Fig. 2). Observed anomalies in December and January were also around or below 0°C, though the warming observed in the southern GBR during these months was not captured by the model ensemble mean. Forecasts for February, however, agreed well with observed conditions.

The GBR Index is the areal average of SST anomalies in the GBR region and has been shown to be a useful indicator of average conditions in the area (Spillman and Alves 2009). The predicted GBR Index ensemble mean showed a steady increase in anomalies from December-May, with the most rapid rise occurring between December and February (Fig. 3). Observed GBR Index values were captured within the ensemble spread for all months shown i.e. the range of the 30 forecasts used to make up the ensemble. Ensemble mean values for January, February and March were all close to those observed. However, December was warmer in reality than the model

¹Bureau of Meteorology Weekly Tropical Climate Note (Accessed: 8 April 2010). Available from

<http://www.bom.gov.au/climate/tropnote/tropnote.shtml>.

climate.tropical@bom.gov.au.

Archived: http://aifsa-nt.bom.gov.au/cgi-bin/cmegi/webdir.showtext.pl?d=/archive/public/2010/04/&f=public_20100406.txt.gz

² Great Barrier Reef Marine Park Authority (Accessed 17 May 2010).

Available from

http://www.gbrmpa.gov.au/corp_site/key_issues/climate_change/management_responses/coral_bleaching_status. bleachwatch@gbmpa.gov.au.

predicted, despite being the first month of the forecast. This may be a result of local atmospheric

events that were not captured by the model.

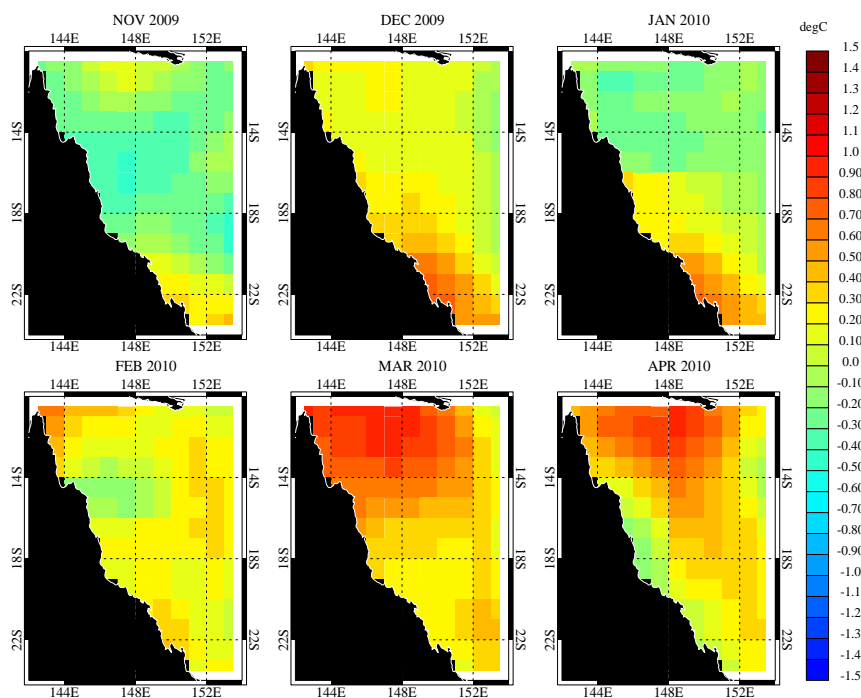


Fig. 1 Monthly Reynolds OI.v2 1°SST anomalies in the GBR region for November 2009 - April 2010.

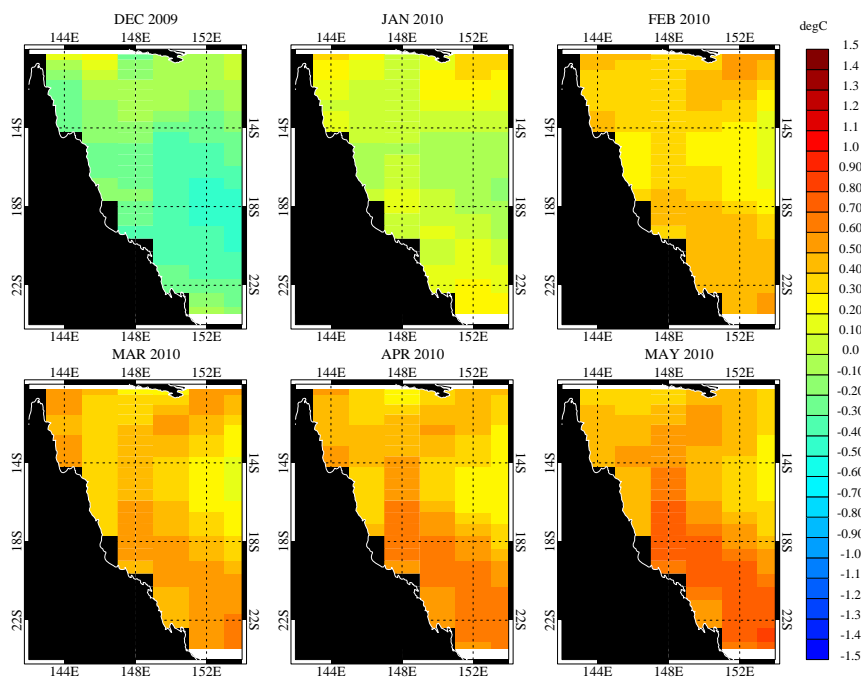


Fig. 2 POAMA SST anomalies (ensemble mean) in the GBR region for December 2009 to May 2010 in the outlook issued on 1 December 2009.

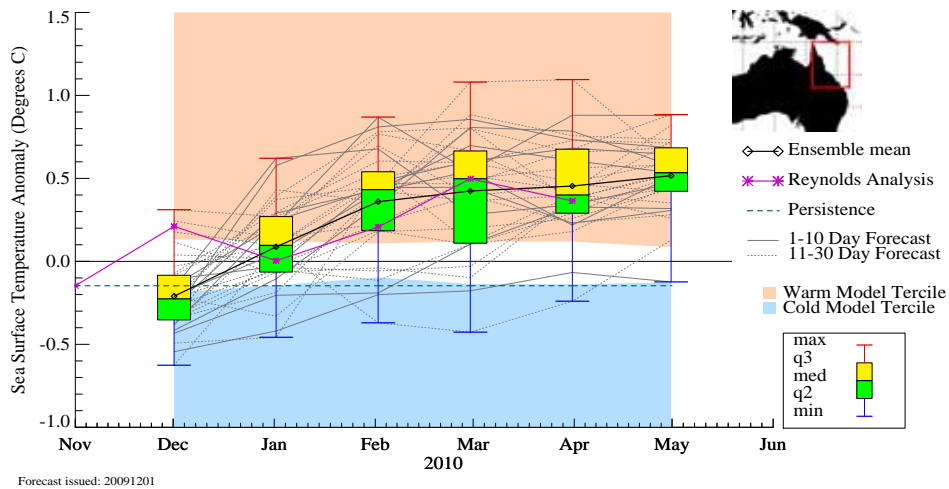


Fig. 3 POAMA monthly GBR Index values for December 2009 to May 2010 in the official outlook issued on 1 December 2009, with the distribution by quartiles of the ensemble composed of the last 30 forecasts. Overlaid is the ensemble mean (black), the observed Reynolds GBR index (pink) and persistence (dashed blue). The shading indicates upper and lower climatological terciles from the POAMA v1.5 hindcasts.

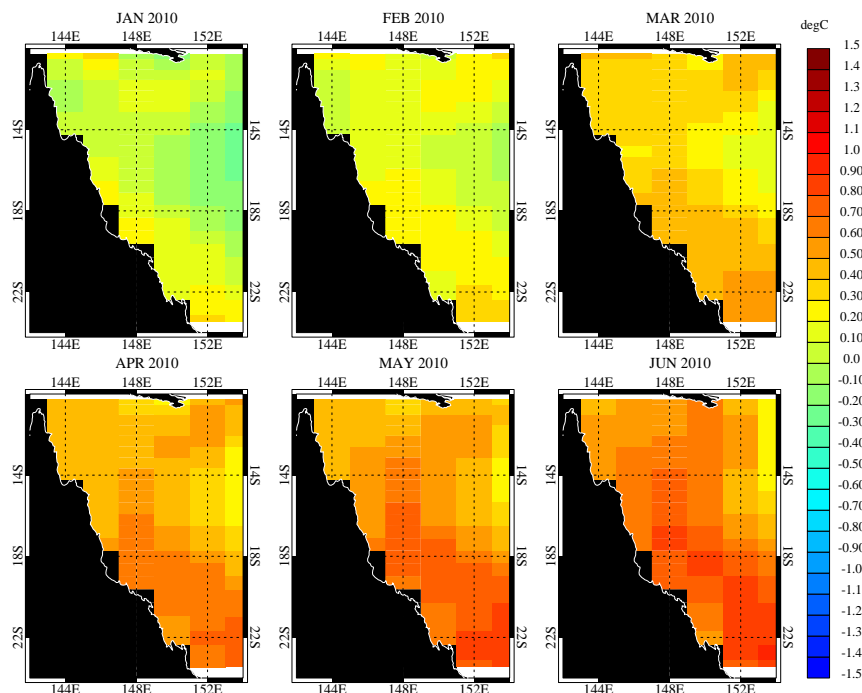


Fig 4 POAMA SST anomalies (ensemble mean) in the GBR region for January- June 2010 in the outlook issued on 1 January 2010.

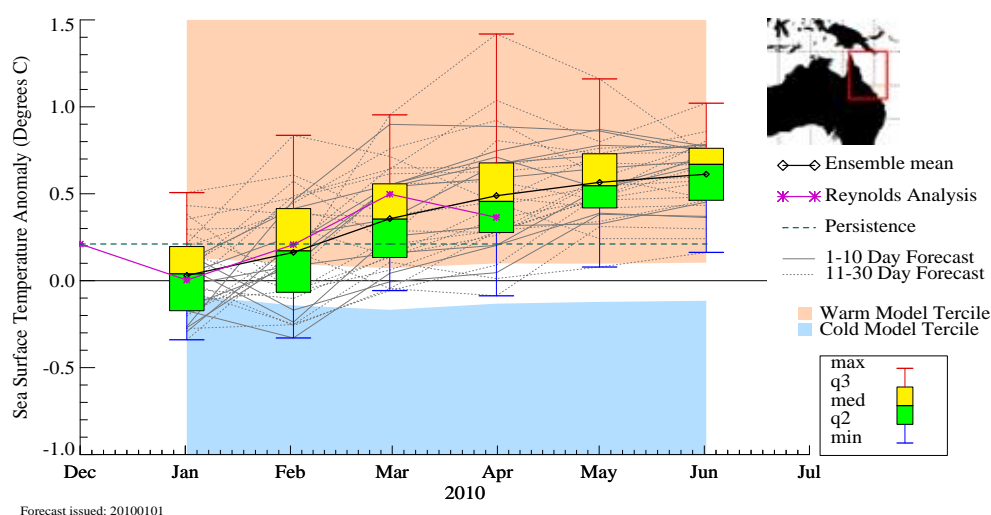


Fig 5. POAMA GBR Index values for January-June 2010 in the outlook issued 1 January 2010, as per Fig. 3.

Forecasts issued in January...

POAMA real-time forecasts issued in January 2010 for January-March 2010 indicated mostly average conditions over the GBR region for January and February, with slight warming occurring in March that increased through to June (Fig. 4). These ensemble mean values agreed well to observed monthly SST anomalies for January and February. Predicted values for March were also comparable to those observed, though the observed warm anomalies in the northern region of the GBR were not captured by the model. However, when considering the probability of SST anomalies exceeding 0.6°C (not shown), forecast probabilities were 0.2-0.3 for March, which indicates that while two-three ensemble members indicated warm anomalies in the north, most did not.

The GBR Index forecast issued in January 2010 for January-June compared very well to observed average SST anomalies in the region (Fig. 5). Ensemble mean values were very close to observed values. Steady warming again was indicated for subsequent months, which agrees well with observed values. The large spread of forecast values for April is mainly due to a single ensemble member forecasting a high monthly anomaly value, with the other members remaining within the spread of other months. The model ensemble members can be interpreted as sampling

different possible future realisations of intraseasonal variability, and large spread usually indicates a limit on our ability to predict the future (Spillman et al. 2009b).

Forecasts issued in February...

Forecasts generated in February for the coming months predicted temperatures close to climatological values for February (Fig. 6). Increased anomalies were forecast for the following months, particularly in the southern GBR in May-July. In February, the model forecast is in very good agreement with observed values (Figs. 1 and 6). Observed values in March and April were warmer than in February, particularly in the northern GBR. Whilst the model predicted warmer temperatures, the location of the higher values was too far south as compared to what was observed. This may either be due to the coarse scale of the model and its ability to capture large scale features, rather than local scale processes. However, these warm conditions are unlikely to be of great concern to reef managers, since the climatological SSTs for those months are lower than for mid-summer meaning that the expected overall temperature to which coral are exposed is lower. The use of anomalies that are referenced to a long-term summer maximum, rather than individual monthly averages, can often be more informative in a bleaching context. To this end, new bleaching forecast products are being

developed and are introduced in the following section.

The ensemble mean forecast for the GBR Index starting in February (Fig. 7) indicated average anomalies between 0.1 and 0.5°C for the following few months. The majority of ensemble

members fell within the upper tercile, particularly the ten most recent members (indicated as solid grey lines). The ensemble means for February, March and April were within 0.1-0.15°C of the observed index values, indicating good agreement.

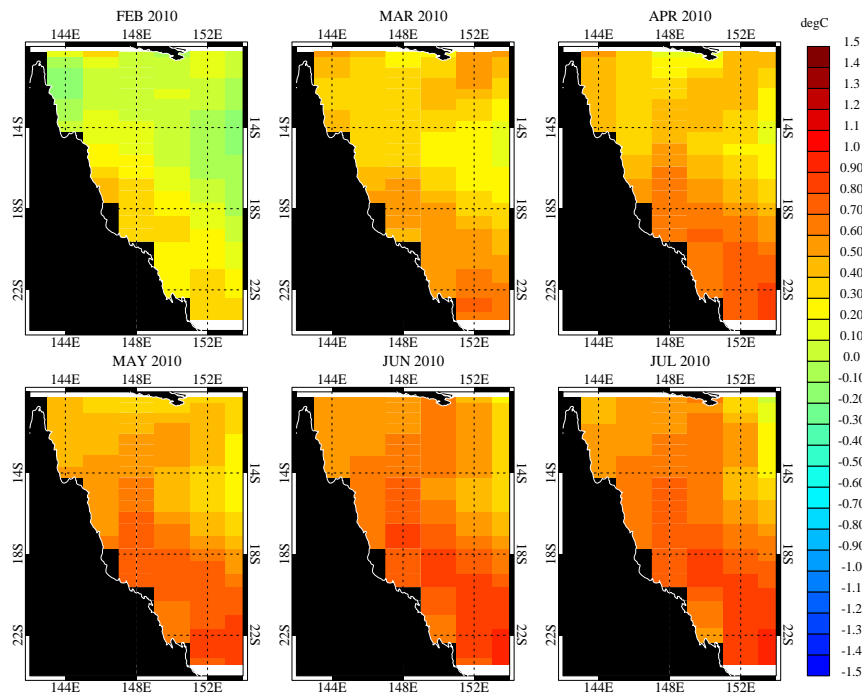


Fig. 6 POAMA SST anomalies (ensemble mean) in the GBR region for February-July 2010 in the outlook issued on 1 February 2010.

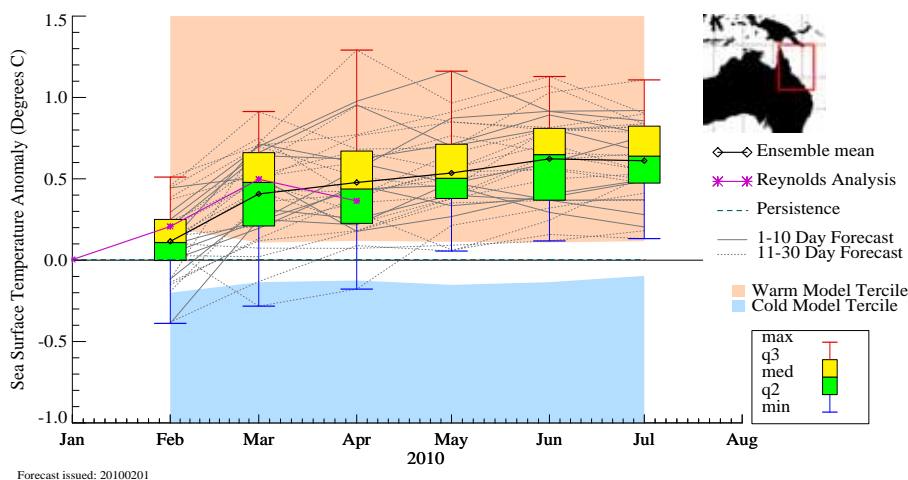


Fig. 7 POAMA GBR Index values for February-July 2010 in the outlook issued 1 February 2010, as per Fig. 3.

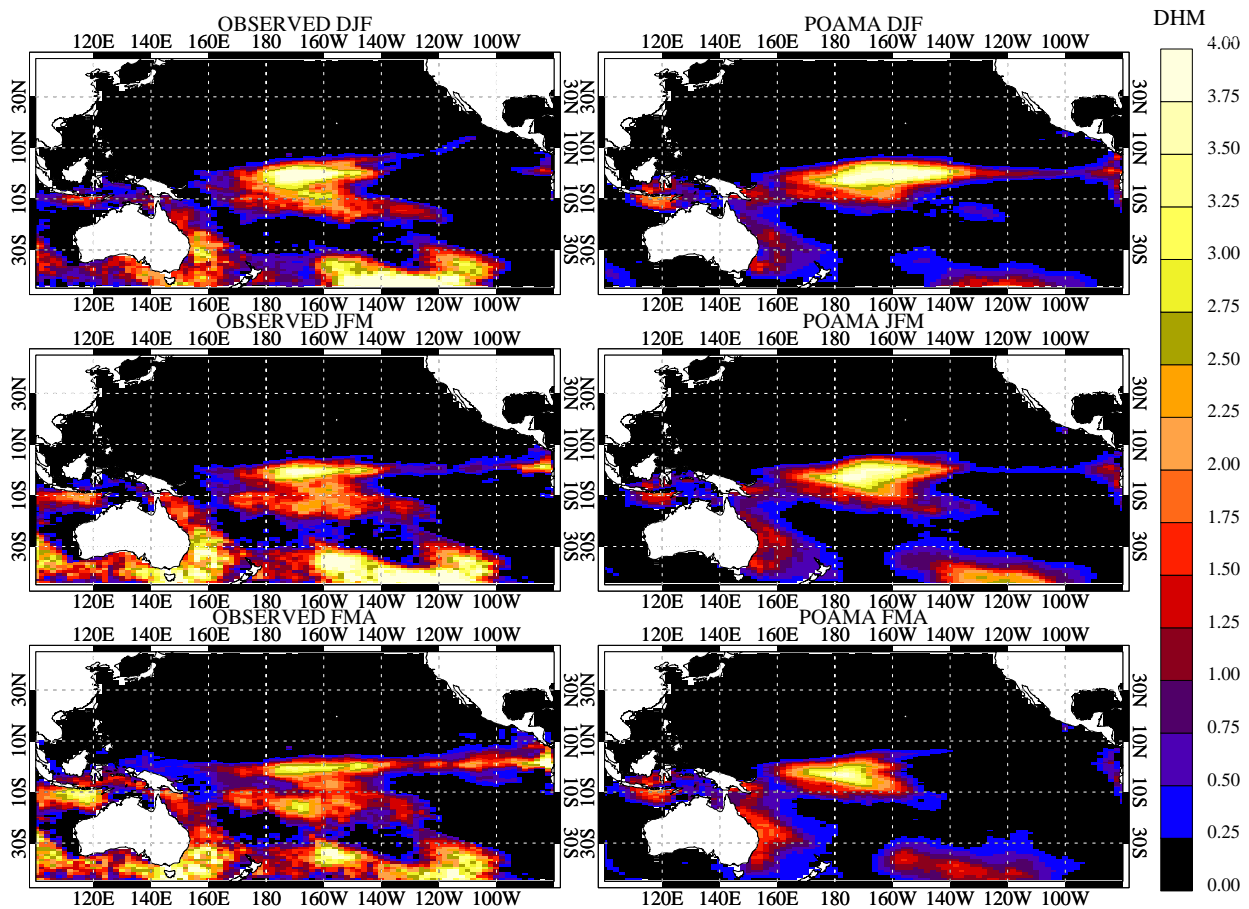


Fig. 8 Observed DHM values (first column) and POAMA ensemble mean DHM forecasts (second column) for outlooks issued on 1 December 2009, 1 January 2010 and 1 February 2010.

New bleaching forecast products

Two new bleaching products using POAMA forecasts are currently under development, based on similar products developed by the NOAA Coral Reef Watch program. Coral HotSpots are a measure of the intensity of thermal stress and are defined as positive SST anomalies referenced to the long term mean temperature of the warmest summer month, or “maximum monthly mean” at a location (Goreau and Hayes 1994; Strong et al. 2004). Degree Heating Months (DHM) give an indication of the persistence of thermal stress and are calculated as the sum of monthly HotSpots $\geq 0^{\circ}\text{C}$ at a location over a rolling three month time period (Eakin et al. 2008; Spillman et al. 2010a; 2010b). Model DHM forecasts were generated by summing over forecasts for the first three months from the outlook issue date i.e. for a forecast issue date of 1 November 2009, HotSpot forecasts for November 2009, December 2009 and January

2010 are accumulated (Spillman et al. 2010a). These products are still experimental, though the current plan is to generate them operationally in time for the summer of 2010/2011.

Model forecasts of DHM values generated on 1 December, 1 January and 1 February compared reasonably well to observed values for the corresponding seasons (Fig. 8). High values in the central tropical Pacific are a result of the persistent ENSO signal and the decay of the event is evident in the gradual decline of DHM values with time. In general, POAMA forecasts for large scale SST events such as ENSO have high skill (Wang et al. 2008), though at smaller spatial scales, intraseasonal variability and local processes can limit prediction skill. Along the north-east coast of Australia in the GBR region, the model predicts moderate DHM values and reproduces the general spatial pattern of the observed DHM values. However it doesn't

capture the amplitude of observed values in the northern GBR, particularly for December-January-February (DJF) and January-March (JFM). This may be due to the impact of local atmospheric processes or model grid resolution limitations. Predicted values on the GBR nevertheless may be sufficiently high enough to cause some concern for reef managers. However, severe coral bleaching on a widespread scale would not be expected, as the peak values are further offshore and much lower than those observed during the mass bleaching event of 2001/2002 ($DHM \geq 3.0$; Spillman et al. 2010a).

Summary

Forecasts from POAMA correctly predicted average conditions in the GBR region for the summer of 2009/2010. During autumn observed warm SST anomalies were also captured by the model, though peak values were often predicted over the southern GBR rather than the northern GBR. When averaged over the region, however, observed values of the GBR Index were captured within the ensemble spread for all months, and within 0.1°C of the ensemble mean for all forecasts. Forecasts of DHM values showed the model predicted the general patterns of thermal stress across the Pacific, particularly in the central tropical Pacific due to a strong ENSO signal. DHM values in the GBR region were elevated, indicating an increased risk of coral bleaching, though not as high as previously observed during mass bleaching events. Only minor coral bleaching was reported during the summer, and was mostly attributed to exposure and rainfall resulting from late January/February 2010 king tides, rather than thermal stress.

References

Baker, A.C., Glynn, P.W. and Riegl, B. 2008. Climate change and coral reef bleaching: An ecological assessment of long-term impacts, recovery trends and future outlook. *Estuarine, Coastal and Shelf Science* 80:435-71.

Bureau of Meteorology. 2010a. ENSO wrap up December 2009-March 2010.

<http://www.bom.gov.au/climate/search/enso-wrap-up.shtml?bookmark=no-rm>

Bureau of Meteorology. 2010b. Seasonal Climate Summary for Queensland: Summer 2009-2010.

<http://www.bom.gov.au/climate/current/season/qld/archive/201002.summary.shtml>

Done, T., Whetton, P., Jones, R., Berkelmans, R., Lough, J.,

Skirving, W. and Wooldridge, S. 2003. Global climate change and coral bleaching on the Great Barrier Reef. Final Report to the State of Queensland Greenhouse Taskforce through the Department of Natural Resources and Mines, p 49.

Donner, S.D., Skirving, W.J., Little, C.M., Oppenheimer, M. and Hoegh-Guldberg, O. 2005. Global assessment of coral bleaching and required rates of adaptation under climate change. *Glob Change Biol* 11:2251-65.

Eakin, C.M., Kleypas, J. and Hoegh-Guldberg, O. 2008. Global climate change and coral reefs: rising temperatures, acidification and the need for resilient reefs In: Wilkinson CR (ed) Status of Coral Reefs of the World: 2008. Global Coral Reef Monitoring Network and Reef and Rainforest Research Centre: Townsville, Australia.

Goreau, T.J. and Hayes, R.L. 1994. Coral bleaching and "ocean hot spots." *AMBIO* 23:176-80.

Goreau, T.J.F. and Hayes, R.L. 2005. Global coral reef bleaching and sea surface temperature trends from satellite-derived hotspot analysis. *World Resources Review* 17:254-93.

Hoegh-Guldberg, O. 1999. Coral bleaching, climate change and the future of the world's coral reefs. *Review. Marine and Freshwater Research* 50:839-66.

Marshall, P.A. and Schuttenberg, H.Z. 2006. A Reef Manager's Guide to Coral Bleaching. Great Barrier Reef Marine Park Authority, Australia pp167 (ISBN 1-876945-40-0).

Maynard, J.A., Johnson, J.E., Marshall, P.A., Eakin, C.M., Goby, G., Schuttenberg, H. and Spillman, C.M. 2009. A Strategic Framework for Responding to Coral Bleaching Events in a Changing Climate. *Environmental Management* 44:1-11.

McClanahan, T.R., Ateweberhan, M., Ruiz, S.C., Graham N.A.J., Wilson, S.K., Bruggemann, J.H. and Guillaume, M.M.M. 2007. Predictability of coral bleaching from synoptic satellite and in situ temperature observations. *Coral Reefs* 26:695-01.

Spillman, C.M. and Alves, O. 2009. Dynamical seasonal prediction of summer sea surface temperatures in the Great Barrier Reef. *Coral Reefs* 28:197-06.

Spillman, C.M., Alves, O. and Hudson, D.A. 2010a. Predicting thermal stress for coral bleaching in the Great Barrier Reef using a coupled ocean-atmosphere seasonal forecast model. *International Journal of Climatology*, *in review*.

Spillman, C.M., Alves, O. and Hudson, D.A. 2010b. Seasonal prediction of thermal stress accumulation for coral bleaching in the tropical oceans. *Monthly Weather Review*, *accepted*.

Spillman, C.M., Alves, O., Hudson, D.A. and Charles, A.N. 2009a. New Operational Seasonal SST Products for Prediction of Coral Bleaching in the Great Barrier Reef.

- Bulletin of the Australian Meteorological and Oceanographic Society 22:112-4.
- Spillman, C.M., Alves, O., Hudson, D.A. and Charles, A.N. 2009b. POAMA SST Predictions for the Great Barrier Reef: Summer 2008/2009. CAWCR Research Letters 2:30-34.
- Strong, A.E., Liu, G., Meyer, J., Hendee, J.C., Sasko, D. 2004. Coral reef watch 2002. Bulletin of Marine Science 75:259-68.
- Wang, G., Alves, O., Hudson, D., Hendon, H., Liu, G. and Tseitkin, F. 2008. SST skill assessment from the new POAMA-1.5 system. BMRC Research Letters 8:2-6.
- Wheeler, M.C., Hendon, H.H., Cleland, S., Meinke, H. and Donald, A. 2009. Impacts of the Madden-Julian oscillation on Australian rainfall and circulation. Journal of Climate 22:1482-14

A discussion on aspects of the seasonality of the rainfall decline in South-Eastern Australia

Bertrand Timbal

Centre for Australian Weather and Climate Research

b.timbal@bom.gov.au

Introduction

Most of South-Eastern Australian (SEA, defined as mainland Australia south of 33.5°S and east of 135.5°E, displayed as a box in Fig. 4) has experienced reduced rainfall since the late 1990s. This was described in detail in Murphy and Timbal (2008) (hereafter MT08) and updated in mid-2009 by Timbal (2009), (hereafter TI09). This note discusses some aspects of the rainfall variability in relation to the on-going decline in light of the summer 2010 wet episode across much of Eastern Australia including SEA.

Above average rainfall in early 2010

During the first months of 2010, while the 2009-2010 El Niño episode was receding rapidly, above average rainfall was recorded in most of Australia. Very large flooding events were observed in inland Queensland with some of that water making its way further south along the Darling River system and into the Menindee Lakes returning the control of the lakes to the Murray-Darling Basin Authority (MDBA) for the first time since 2002 (MDBA, 2010). While the most significant rainfall events were located in inland tropical regions, some of these extended further south affecting SEA. Regional averages were above long-term averages in both February (82.4 mm compared to a mean for the 20th century of 36.6 mm) and March (67.0 mm compared to a mean of 40.7 mm).

The February total is particularly significant. This is the first very wet month (as defined as being above the 90th percentile of the monthly climatology) since January 1995 (Fig. 1) interrupting a run of 180 months in a row with monthly total rainfall below the 90th percentile.

This perspective of the on-going rainfall deficiency illustrates that it is made of below

average rainfall and very low natural variability as described in MT08 and in this regard it is different from previous dry periods such as 1935-1945 during which very wet months were recorded, albeit not as frequently as wetter epochs such as the 1950s and 1970s.

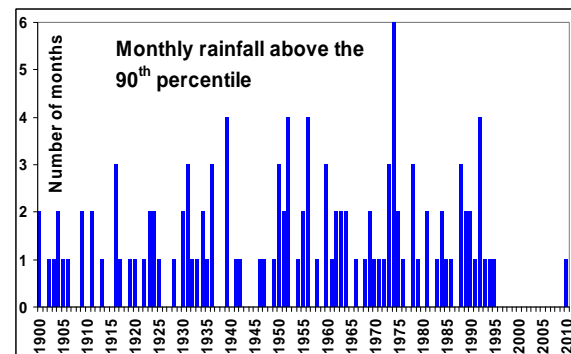


Fig. 1 Number of months per year with rainfall above the 90th percentile (updated to July 2010). Percentiles are based on the 20th century (1900-1999) climatology and are computed month by month.

It is noteworthy that the last two very wet months (above the 90th percentile) were in summer, a season where the rainfall decline is the smallest (TI09). In contrast, the last recorded very wet months in autumn occurred in 1990, in winter it was in 1991 and in spring in 1993. These are three seasons with observed rainfall decline (TI09). In this regard, the above average March total rainfall, while not as significant in percentile terms is interesting as it affects the first month of the continuum from March to October with observed rainfall decline since 1997 (Fig. 2).

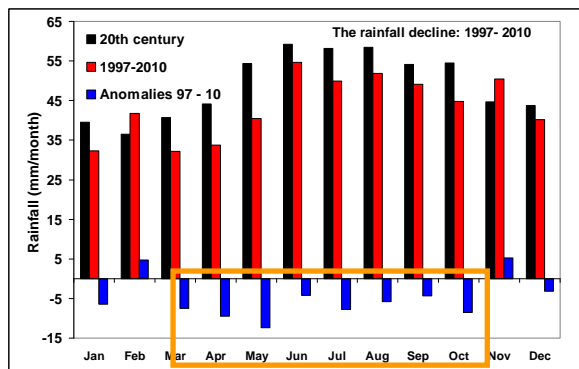


Fig. 2 Monthly mean SEA rainfall for the 20th century climatology (1900 to 1999) (black bars) and for the on-going rainfall deficit period (from January 1997 to July 2010). Changes from the long-term climatology are shown as blue bars. The continuous months with negative rainfall since 1997 are outlined with orange boxes.

The wet 2010 March contributes to reduce the “season paradox” in the on-going rainfall decline in SEA: on one hand, the observed rainfall decline is predominantly an autumn phenomenon, although decline in winter and spring have become more sizeable recently (TI09); on the other hand, future climate projections in response to anthropogenic forcings point also to a rainfall decline across these three seasons that is largest in spring followed by winter and smallest in autumn (BoM and CSIRO, 2007). While there is a growing confidence in the possibility of attributing at least part of the on-going rainfall decline in SEA to global warming and thus anthropogenic emissions (CSIRO, 2010), the seasonality of the current decline remains troublesome. The only formal external attribution study of the on-going rainfall decline in SEA (Timbal et al. 2010) suggests that while recent observed rainfall decline in winter and spring is not inconsistent with the model response to anthropogenic external forcings, the observed decline in autumn is twice larger than the mean model response suggesting that for this particular season, a large part would be due to naturally occurring variability.

In light of the wet March 2010 and the season paradox it is worth evaluating the annual cycle of natural variability and its relation if any with the seasonality of the on-going rainfall deficiency.

Rainfall variability versus rainfall decline

The standard deviation (STD) of monthly rainfall was computed using the 20th century climatology (Fig. 3). It varies in a small range between a low of 20 mm in September and a high of 27 mm in May. Once the STD is normalised by the monthly mean climatology, there is a marked seasonal cycle peaking in February (above 70 percent) and bottoming in July below 35 percent. From this perspective, the month of March belongs to the group of months centred on the warmest part of the year with the largest rainfall variability. The decline of this ratio is sharp across autumn and then lingers below 40 percent from June to September. There is a clear separation between the highly variable warm months and the less variable cool months.

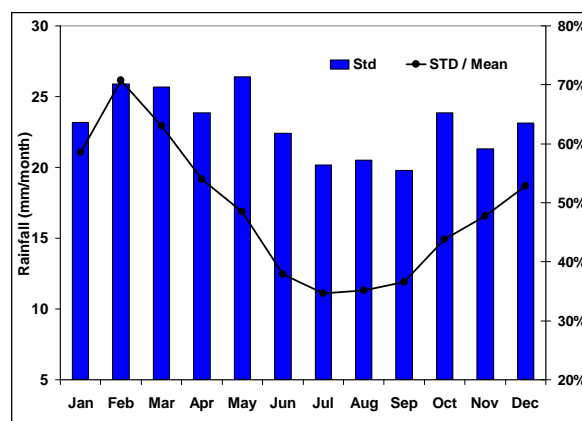


Fig. 3 Monthly standard deviations for SEA rainfall during the 20th century (blue bars) normalised by the monthly means (shown in Fig. 1). The Y-axis for raw STD is shown on the left (in mm/month), and on the right for the normalised values (in %).

Given these observations, one is led to wonder if natural variability contributes to the magnitude of the on-going deficiency. This is evaluated by relating the magnitude of the absolute rainfall deficit and the standard deviation (STD) for each month. Correlations were calculated both in absolute terms and in percentages of the 20th century monthly climatology (Table 1). As a first guess, up to 70 percent of the magnitude of the rainfall decline for a particular month from March to October can be traced back to how variable that monthly rainfall was during the 20th century. With the other four calendar months these correlations collapse to insignificant values. The rationale for limiting this correlation to eight

months instead of the full year is that we are only interested in the months that have a significant relationship with the Sub Tropical Ridge Intensity (STR-I) and hence a response to its increase (Timbal et al. 2010). The drawback is that, with only eight numbers considered; correlations need to be above 0.84 to be significant at the 99 percent level. This is the case when the rainfall deficit is expressed as a percentage of the long-term climatology.

Table 1: Correlation coefficients between monthly 1997-2009 rainfall deficit and monthly 20th century rainfall variability for the 8 individual months from March to October (numbers in brackets are for the twelve calendar months). Bold (italic) figures are significant at the 99% (95%) level.

Pearson correlation Coefficient		1997-2009 rainfall deficit	
		Absolute (mm)	Percent
20 th century rainfall variability	STD (mm)	0.81 [0.33]	0.85 [0.36]
	STD / mean (%)	0.67 [0.11]	0.85 [0.01]

The annual cycle of the normalised variability of rainfall is counter-intuitive. Natural variability is lowest from June to September, the time of the year where well known modes of variability in the Pacific (McBride and Nicholls 1983) and Indian (Nicholls, 1989) equatorial oceans, as well as at the higher latitudes (Hendon et al. 2007), have the strongest influence on SEA rainfall. The lack of relationships in these modes in autumn (Timbal and Murphy 2007) is puzzling considering that apart from February, the inter-annual STD is largest for the autumn months.

Therefore it is important to differentiate between natural variability attributable to known modes of variability (i.e. *organised natural variability*) and un-explained (at this point in time in our understanding of SEA rainfall variability) or *random natural variability*, which both contribute to the total natural variability. From a purely statistical point of view, known modes of variability appear to constrain random natural variability and reduce overall natural variability in winter and spring. On the contrary, in the absence of relationship between rainfall and known modes of variability (in summer extending to autumn) natural variability of

rainfall is largest.

Annual cycle of daily rainfall

Having observed that rainfall variability is largest at the time of the year when unexplained or random variability is largest; it is interesting to extend this discussion using daily rainfall, which is the relevant scale to evaluate the weather noise. Daily rainfalls at four locations scattered across the SEA area of rainfall deficiency (Fig. 4) are used. Two wet coastal locations (Robe averaging 641 mm/year and Melbourne, 648 mm/year) and two dry inland locations (Wentworth, 283 mm/year and Deniliquin, 404 mm/year) were chosen to sample the spatial variability of rainfall climatology across SEA. The choice of the locations was also based on the availability of the longest possible daily records. These records ranged from 137 years in Wentworth to 155 years in Melbourne. The statistics used can be extracted from the BoM external web site: http://www.bom.gov.au/climate/averages/index.shtml?map_type=cdio&code=3

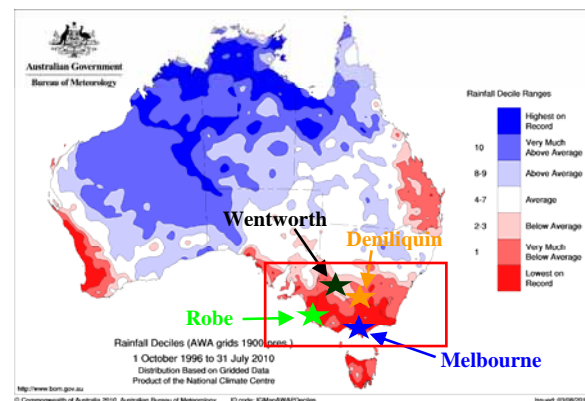


Fig. 4 Total rainfall deciles across the Australian continent for October 1996 to July 2010 (updating Fig. 1 in TI09). The four locations for which daily rainfall statistics are displayed in Figs. 5 and 6 are shown. The box used to define south eastern Australia is shown in red.

In all four locations, record daily rainfall occurred during a dry warm month (December, February or March) (Fig. 5). Interestingly, the four sites rank in the exact opposite order for the largest values compared with mean climatology: i.e. the largest 24-hour rainfall was recorded in Wentworth (172 mm on 8 February 1911) the driest of the four sites. Not surprisingly an attempt to normalise daily extreme rainfall by the

monthly mean climatology increases these differences. Largest daily rainfall can be up to eight times the monthly mean (in the case of Wentworth in February, NB: in the left panel of Fig. 5, percentages in excess of 400 percent are truncated in five instances). Contrary to summer extreme daily rain totals, winter ones tend to be largest in the coastal wet locations (Melbourne and Robe).

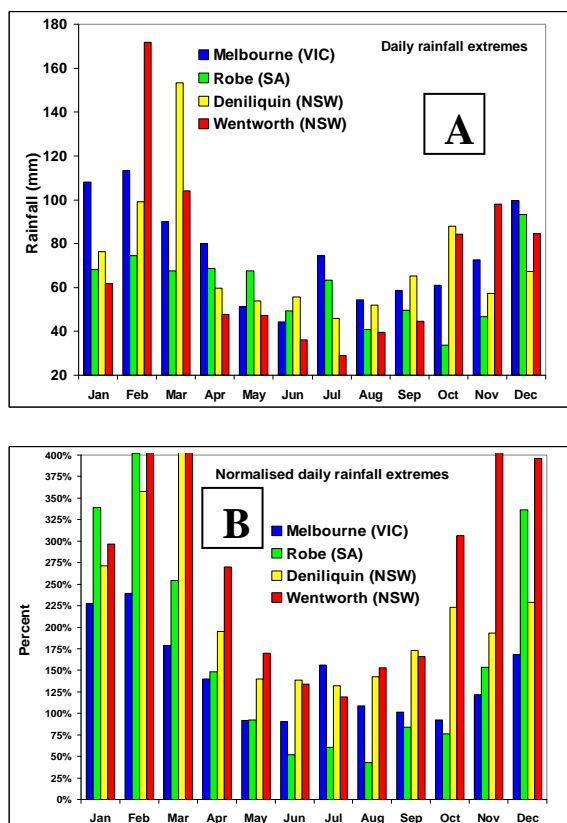


Fig. 5 Largest observed daily rainfall for each calendar month recorded at four locations across SEA, in absolute term (mm) (A) and in percentage of the monthly mean values (B). NB: percentage above 400% (and up to 800%) in the right graph were truncated. The length of the observation record varies across the four locations between 137 and 155 years.

An additional aspect of the annual cycle of daily rainfall is the number of rain occurrences (rainfall recorded above 0.2 mm). In all four locations across SEA (Fig. 6), there is a clear annual cycle with the number of rain days per month peaking in winter (June-July-August). Once normalised by the annual total rainfall recorded locally, the similarity between the four locations is even more striking. The annual cycle of how rain days

at any of the SEA locations are spread across the year are very similar and are independent of local climate. This consistency in the annual cycle of rain days across SEA once normalised (right panel in Fig. 6) is in sharp contrast to the largest rain day amount (right panel in Fig. 5).

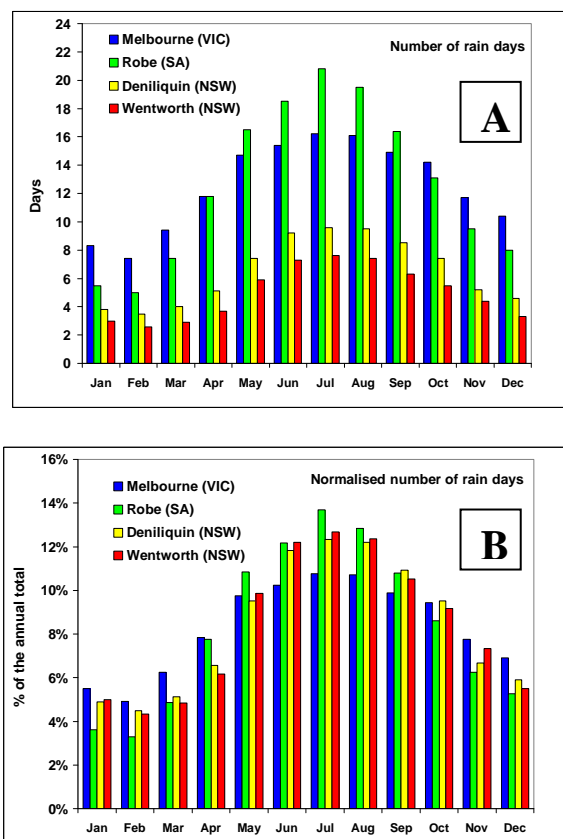


Fig. 6 Numbers of rain days (above 0.2mm) recorded at four locations across SEA, in absolute term (A) and as a percentage of the annual mean total number of rain days (B). The length of the observation record varies across the four locations between 137 and 155 years.

The picture emerging from these daily rainfall statistics is that monthly winter rainfall consists of many rainfall days with few extreme rain events. This nature of winter rainfall is consistent across the SEA region for both wet and dry locations. Therefore, a variation in the weather noise (i.e. the number of rain bearing systems affecting SEA) will have a relatively small effect on monthly totals and hence the total inter-annual variability will be small despite the remotely controlled part of the variability being significant. On the contrary, monthly summer rainfall is far more erratic and made of fewer rain occurrences.

Therefore, the total monthly rainfall can vary considerably from one year to another simply due to a small change in the number of rainfall events, leading to a lesser statistical significance for a similar magnitude of decline. This behaviour is accentuated inland in the dryer locations. The period exhibiting rainfall deficiency currently is predominantly in the winter-type category although the early part of autumn (i.e. March) is more summer-like from this perspective and hence the magnitude of the on-going decline for this month is more likely to be influenced by weather noise variability. This finding is consistent with the fact that for March, little rainfall decline was anticipated based on the observed STR changes (Timbal et al. 2010).

Is the month of June special?

Away from the more variable part of the annual cycle of rainfall, June has interesting characteristics which set it apart from the other cool months. When using the accepted World Meteorological Organisation (WMO) standard 1961-1990 as a reference period, there was no rainfall decline in June (MT08). Despite being the WMO standard, 1961-1990 is amongst the wettest 30-year periods on record and thus has been abandoned as a suitable reference period for SEA. When the entire historical record from 1900 is used (Fig. 2), June like other winter months exhibits a rainfall decline. Nevertheless it remains the smallest rainfall decline over the March-October continuum.

MT08 results can be explained by looking at the wet period 1961-1990 (Fig. 7). June has above average rainfall in contrast to most other months (all months from April to October are currently experiencing rainfall deficits). The fact that 1961-1990 is markedly above the long-term average is a reminder that using rainfall trends starting within this period is unwise as it compounds the on-going rainfall decline with an anomalous wet period. This wet period followed a significant and well known upward shift in the late 1940s (Nicholls et al. 1997); in the case of SEA it delimits two epochs: a dryer one between the 1900s and 1940s and a wetter one from the 1940s to the 1990s (MT08).

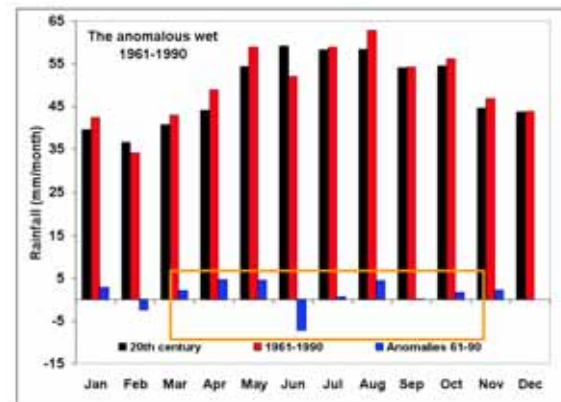


Fig. 7 Monthly means SEA rainfall for the 20th century climatology (1900 to 1999) (black bars) and the W.M.O. reference period from 1961 to 1990 (red bars); changes from the long term climatology are shown as blue bars. The continuous months with negative rainfall since 1997 are outlined with orange boxes.

The fact that June rainfall anomalies since 1997 are lower than for the other months in terms of rainfall decline is consistent with the relationship between natural variability for each calendar month and the magnitude of the decline discussed earlier. June was observed to have low inter-annual variability in percentage terms (Fig. 3); it stands out as the calendar month with the lowest range between the 20th and 80th percentile despite having the largest mean rainfall (Fig. 8). This is even more so for the 10th to 90th range (not shown). The fact that June is the month with the highest 20th percentile is likely to contribute to the small June rainfall deficit over the last thirteen years. In six instances, annual rainfall was in the lowest 20th percentile (2.6 would be the expected number for a random period). Going back to the daily extreme rainfall (Fig. 5), the month of June also stands out as the time of the year with the lowest (Melbourne) or second lowest (all three other locations) daily rainfall extreme in percentage of the monthly climatology. It is however difficult to argue that June is special in that regard since arguably, that statistic is similar across all cool months from May to September.

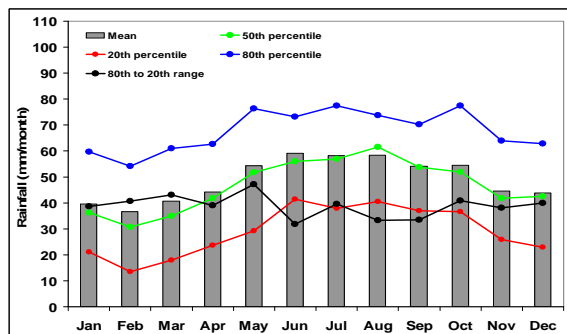


Fig. 8 Monthly mean (grey bars), median (green line), 20th and 80th percentiles (red and blue lines) as well as the 80th -20th percentile range (black line) for SEA rainfall during the 20th century (in mm/month).

Finally, it is worth noting that the negative anomaly in June for the period 1961-1990 is unlikely to be explained by the relatively low 80th percentile compared to the other wet months. A more in-depth investigation would be required but this is outside the scope of this discussion where the focus is on understanding the on-going decline.

Concluding remarks

In this note, the observed natural variability of SEA rainfall was discussed. It was seen that the magnitude of the monthly rainfall deficiency during the March to October period appears related to the magnitude of the inter-annual variability of that monthly rainfall. This relationship is strong and significant, despite the very small sample size but decreases dramatically as soon as the other calendar months are considered. The sudden jump is not necessarily evidence that this relationship is coincidental since it was anticipated based on the STR-I rainfall relationship across SEA, which is insignificant during the warmer months and is understood to be a key mechanism that explains the on-going rainfall deficit (Timbal et al. 2010).

In this regard, the wet start of 2010 should not be considered as a drought breaking event. February 2010 is remarkable since it ended a spell of 180 months without a high (above the 90th percentile) monthly total. This is consistent with the highly variable nature of summer rainfall, which was noted to extend to March. The wet month of March 2010 has contributed to reduce the magnitude of the autumn rainfall decline since

1997, thus reducing the season paradox between the observed rainfall decline and the projected one in response to anthropogenic forcings. It has also contributed to reduce the discrepancy between the annual cycles of the expected rainfall decline due to the STR intensification compared to the observed one which is largest in March (Timbal et al. 2010). It is also consistent with an attribution study, which found that it is in autumn where the rainfall decline due to natural variability is most likely to be largest compared to the part that is a response to global warming

This note also sheds some light on the intriguing case of June identified by MT08 as the only cold month with no rainfall decline. This is due to a combination of using the 1961-1990 WMO reference period and the fact that rainfall in June is composed of a large number of low rainfall days leading to a resilient month with limited inter-annual variability and in particular when it comes to low rainfall years (in the lowest 20th percentile), which have been numerous in the recent dry period.

It is now well documented that it is not a naturally occurring mode of variability that is driving the rainfall decline in SEA (CSIRO, 2010). Whilst the seasonality of rainfall decline has been strongly linked to the seasonality of the STR-I influence on rainfall (Timbal et al. 2010), it was observed here that the month by month magnitude of the decline relates closely to the overall magnitude of the decline pointing to random variability as a contributor to the seasonality of the decline and hence the season paradox described earlier.

Finally, some of the observations made here regarding the annual cycle of inter-annual variability of SEA rainfall are simple checks applicable to climate models to help evaluate their ability to provide meaningful future rainfall projections. In particular, it may be possible to evaluate the models ability to reproduce the various processes governing SEA rainfall variability, known modes of variability and weather noise. Understanding this may help answer why the on-going deficiency (partly linked to global warming) is predominantly an autumn decline while future projections are predominantly pointing toward a winter/spring

decline. Also, using the line of argument that the strengthening of the STR is shifting rain-bearing systems further south reducing their impact across SEA, it is possible to think that the ongoing rainfall decline is a shift of the dryer inland climate further south. Pushing this analogy further, the observations that distributions of raindays are insensitive to total rainfall amount while largest rainfall events are higher in dryer locations open up the possibility that as SEA climate is becoming dryer, more intense rainfall has the potential to occur not only in summer in absolute terms but all year around in relative terms. To evaluate this hypothesis will require an analysis of climate model rainfall projections.

While the analysis of SEA monthly rainfall variance in GCM may be a relatively simple endeavour (with the caveat that the small extent of the observed area of decline is described by very few number of grid cells in typical GCMs), the analysis of daily rainfall characteristics from the same models is likely to be very challenging considering the known biases of daily rainfall in GCMs.

Acknowledgements

This communication arises from the involvement of BT in the South-Eastern Australian Climate Initiative (SEACI). The support of the funding agencies is acknowledged. DewiKirono and Pandora Hope have made useful comments to improve an earlier version of this communication, as well as the Editor Paul Sandery.

References

- Bureau of Meteorology and CSIRO. 2007. Climate Change in Australia, Technical Report, Australian Greenhouse Office. www.climatechangeinaustralia.gov.au, 148 pp
- CSIRO. 2010. Climate variability and change in south eastern Australia - A synthesis of findings from Phase 1 of the South Eastern Australian Climate Initiative (SEACI), SEACI report, 36pp, available on-line at: <http://www.seaci.org>
- Hendon, H.H., Thompson, D.W.J. and Wheeler, M.C. 2007. Australian rainfall and surface temperature variations associated with the Southern Annular Mode, *J. Climate*, **20**, 2452-67
- McBride, J.L. and Nicholls, N., 1983. Seasonal relationship between Australian rainfall and the Southern Oscillation, *Mon Wea Rev*, **111**: 1998-2004
- Murray-Darling Basin Authority (MDBA). 2010. Basin agreement rules applied as Authority assumes control of Menindee lakes water, MDBA press release, 12th April 2010, on-line at: <http://www.mdba.gov.au/files/Assuming-control-of-menindee.pdf>
- Murphy, B. and Timbal, B. 2008. A review of recent climate variability and climate change in south-eastern Australia, *Int J Climatol*, **28**(7), 859-79
- Nicholls, N. 1989. Sea surface temperatures and Australian winter rainfall, *J of Clim*, **2**, 965-73
- Nicholls, N., Drosowsky, W. and Lavery, B. 1997. Australian rainfall variability and change. *Weather*, **52**(3), 66-71.
- Timbal, B. and Murphy, B. 2007. Observed climate change in South-East of Australia and its relation to large-scale modes of variability, *BMRC Res Let* **6**, 6-11
- Timbal, B., Arblaster, J., Braganza, K., Fernandez, E., Hendon, H., Murphy, B., Raupach, M., Rakich, C., Smith, I., Whan, K. and Wheeler, M. 2010. Understanding the anthropogenic nature of the observed rainfall decline across South Eastern Australia, *CAWCR Tech.Rep.*, **26**, 180pp: http://www.cawcr.gov.au/publications/technicalreports/CTR_026.pdf
- Timbal, B. 2009. The continuing decline in South-East Australian rainfall – Update to May 2009, *CAWCR Res. Let.*, **2**, 8pp.

Evaluation of ACCESS-A Clouds and Convection using Near Real-Time CloudSat-CALIPSO Observations

A. Protat, L. Rikus, S. Young, J. Le Marshall, P. May, and M. Whimpey

Centre for Australian Weather and Climate Research (CAWCR), Melbourne, Australia

a.protat@bom.gov.au

Introduction

The importance of clouds on climate through their direct effect on the Earth radiation budget and water cycle is well recognized. Clouds and their interaction with incoming and outgoing radiation remain the largest source of uncertainty among future climate projections produced by climate models (e.g. Bony et al. 2006; Dufresne and Bony 2008). The way clouds are represented in numerical weather prediction (NWP) models also significantly affects the quality of weather forecasts (e.g. Jakob 2002). The representation of deep convective systems and associated rainfall is also still a major challenge for NWP models, as there is growing evidence that NWP models produce way too many events but characterized by too little rainfall.

The A-Train satellite mission (Stephens et al. 2002) offers new and unique opportunities to evaluate NWP models at global and regional scales, and for different weather regimes. As part of the A-Train, the 95 GHz cloud radar onboard CloudSat and the dual-wavelength lidar onboard the Cloud-Aerosol Lidar Infrared Pathfinder Satellite Observations (CALIPSO, Winker et al. 2009) satellite provide a vertically-resolved description of the geometrical and microphysical properties of clouds and convection, which is crucial for model evaluation, as illustrated in Illingworth et al. (2007). In the present paper we describe a platform for the evaluation of clouds and convection generated by the regional and limited-area versions of the operational Australian NWP system (ACCESS) using near real-time products of the CloudSat and CALIPSO mission. The potential of this platform for model verification and for the evaluation of products assimilated by models is highlighted using the case study of Tropical Cyclone Olga (28/01/2010). More of these co-located model

and observation samples are currently being produced in order to produce robust skill scores to be compared with scores of other models (e.g. Hogan et al. 2009). It is envisaged that more models could join in the same way as described for the Cloudnet project in Illingworth et al. (2007).

The CloudSat-CALIPSO near real-time hydrometeor mask

The CloudSat and CALIPSO missions release near real-time products that are accessible to the science team members. These products have been rarely used so far. These products are:

- the CloudSat 1B-CPR-FL product, which contains backscattered power and radar information, from which radar reflectivity can be calculated. This product is typically available 4 to 8 hours after collection (e.g. Mitrescu et al. 2008) at the Cooperative Institute for Research in the Atmosphere (CIRA) Cloudsat Data Processing Center.
- the CALIPSO “expedited” Level 2 Vertical Feature Mask (VFM) products (Vaughan et al. 2009), which contains an expedited version of the official cloud and aerosol mask derived from the lidar backscatter measurements. This product is available from the Atmospheric Science Data Center at NASA Langley.

The main drawback of these near real-time fields is that they use a climatological representation of the atmosphere and forecasts of the satellite tracks rather than actual meteorology and tracks, which could cause occasionally layers to be missed or falsely detected. A combined CloudSat-CALIPSO hydrometeor (from clouds and convection) mask named 2B-GEOPROF-LIDAR is produced operationally at CIRA (Mace

et al. 2009), but with a typical one to two weeks latency (if not more), because it uses as inputs the latest officially-released versions of the mission products described just above. Therefore, in order to build a continuous and near real-time platform for the evaluation of clouds and convection in models, a hydrometeor mask using the expedited versions of these products has been produced in this study, following the recommendations of Mace et al. (2009). First the CloudSat mask is produced, by calculating the radar reflectivities from the raw information and extracting the meteorological signal from the measurement noise. These radar reflectivity profiles are then

merged with the CALIPSO-derived cloud base and top heights to produce a CloudSat-CALIPSO hydrometeor mask. It is noteworthy that as in Mace et al. (2009) the highest vertical resolution of the lidar (60 m, as compared to 240 m for CloudSat) is retained for cloud base and top height estimates. This point is particularly crucial for low-level clouds. When compared with a model, the model levels and horizontal resolutions are used to compute a “model-equivalent” hydrometeor mask and hydrometeor fraction from these higher-resolution observations (see Illingworth et al. 2007 for further explanations).

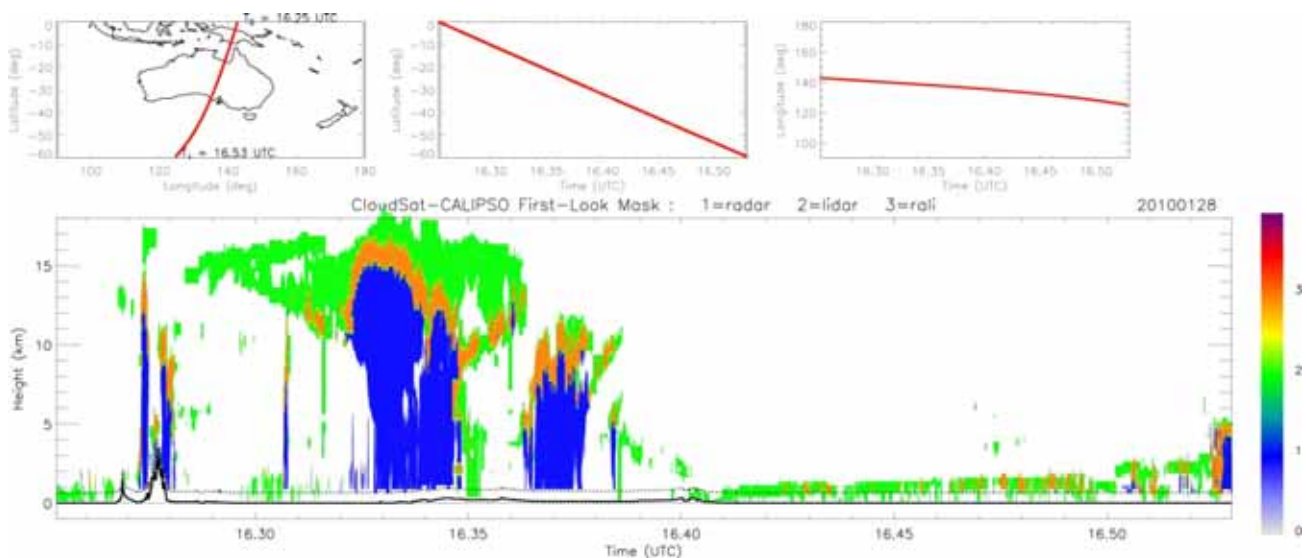


Fig. 1 The near real-time CloudSat-CALIPSO hydrometeor mask on 28/01/2010 through Tropical Cyclone Olga. Green part is detected by lidar only, orange by both radar and lidar, and blue by radar only. The orbit track in the ACCESS domain is given in the upper-left panel. Latitude-time and longitude-time plots are also given. Note that times are given as decimal hours throughout this paper.

An illustration is given in Fig. 1 for a CloudSat-CALIPSO orbit through Tropical Cyclone Olga on 28 January 2010. The first striking result to note from this figure is the wealth of information that can be used for model verification for different types of clouds using a single orbit: land-based and oceanic deep convective systems at different latitudes, “warm” convection, mid-level clouds detrained from the deep convective systems, tropical and mid-latitude thin and thick cirrus clouds, low-level drizzling and non-drizzling stratocumulus clouds, etc ... For this particular day, nearly every type of tropical, subtropical, and mid-latitude cloud has been sampled in the eight orbits over the Australian region. The

second important fact illustrated by Fig. 1 is the synergy between cloud radar and lidar observations. Typically, cloud radars such as CloudSat penetrate most cloud and precipitation layers (see blue regions in Fig. 1) except most intense convective storms producing rainfall rates of 8 mmh^{-1} or more, but will miss a significant portion of the thin cirrus clouds (Comstock et al. 2002; Protat et al. 2006). Conversely, lidars such as CALIPSO will detect these thin cirrus clouds (see green regions above 10 km height in Fig. 1), but the backscatter signals will often be extinguished by super-cooled liquid cloud layers in mixed-phase clouds or clouds of optical depth larger than 2 to 3 (e.g. Sassen and Cho 1992).

There is an overlap region in which radar-lidar observations can be used simultaneously to derive accurate retrievals of cloud properties (e.g. Donovan et al. 2001; Tinel et al. 2005; Delanoë and Hogan 2008). However, it has been estimated that this overlap only corresponds to about ten-twenty percent of the total ice cloud volume of mixed-phase and ice clouds (Illingworth et al. 2007). Fig. 1 is also a good illustration of this point, with relatively small fractions of orange regions when compared with the blue and green regions. The synergy of cloud radar-lidar measurements is clearly recognized as the most accurate (and only) characterization of the vertical distribution of hydrometeors in the troposphere. It is to be noted however that some hydrometeors could remain undetected by the cloud radar-lidar combination, essentially when the lidar beam is extinguished while the cloud radar is not sensitive enough (the top and base of low-level stratocumulus when a thick ice cloud lies above, for instance). The frequency of occurrence of these situations is unknown.

The ACCESS-A model version

The model outputs used in this study are from the parallel trial of the Australian regional mesoscale model (ACCESS-A) which is based on the UKMO Unified Model system. The domain extends from 55°S to 4.73°N in latitude and from 95°E to 169.7°E in longitude with a horizontal resolution of 11 km and 50 height levels in the vertical. The model is run four times a day with full 4DVAR assimilation and produces hourly forecasts out to two days. Clouds are produced by a diagnostic scheme with triangular probability function (Smith 1990). A critical relative humidity criterion is parameterized, assuming a width of PDF dependent on local variability of temperature and moisture (Cusack et al. 1996, 1999b). The vertical gradient cloud scheme of Smith et al. (1999) is used. The microphysics scheme is a mixed phase scheme including prognostic ice water content, and solves physical equations for microphysical processes using particle size information (Wilson and Ballard 1999). Convection is produced by a mass flux scheme based originally on Gregory and Rowntree (1990), but with major modifications including convective momentum transport based on flux gradient relationship, separate deep and shallow schemes, and inclusion of a simple radiative representation of anvils.

ACCESS-A Evaluation

On 28/01/2010, Tropical Cyclone Olga caused some severe damage in Northern Australia. As shown in Fig. 1, the CloudSat-CALIPSO orbit crossed this cyclone, and it crossed it a second time later (not shown). In order to compare model and observations, the horizontal and vertical resolutions of the model have been used to generate a “model-equivalent” hydrometeor mask from the original mask shown in Fig. 1. This “model-equivalent” CloudSat-CALIPSO hydrometeor mask is shown in Fig. 2a together with the corresponding hydrometeor mask derived from the corresponding ACCESS-A forecasts for different lead times (T+4h, T+16h, T+28h, T+40h, Figs. 2bcde, respectively).

For this particular case, the model seems to reproduce most of the clouds and convective systems along the orbit, which is very encouraging. The tropical cyclone (most active part located between $t=16.32\text{h}$ and $t=16.36\text{h}$ on Fig. 2) is present at all lead times in the ACCESS-A simulation, with varying shapes but roughly the same correct location. It is observed that the vertical extent of the tropical cyclone is a few kilometers lower than the observations. It is also clearly seen that the model predicts much less cirrus clouds detrained from the tropical cyclone than observed. The two external convective bands (as one moves further out of the cyclone eye, around $t=16.28\text{h}$ and $t=16.37\text{h}$) are also present in the ACCESS-A simulations and with a correct location. However it is clearly seen that the observed convective band at $t=16.37\text{h}$ is clearly producing rainfall, which is not the case in the ACCESS-A simulation at all forecast lead times. This is also the structure that has the largest variability amongst the different lead times. The low-level stratocumulus and cumulus clouds observed over the ocean off the south coast of Australia are also clearly well reproduced by ACCESS-A at all forecast lead times. It is to be noted however that the simulated low-level cloud layer seems to be thinner than observed, which will require further studies when more model simulations become available. Finally a slight overestimation of ice cloud cover is observed in the region from $t=16.47\text{h}$ to $t=16.49\text{h}$ at around 5 km, where observations show just some short-lived clouds.

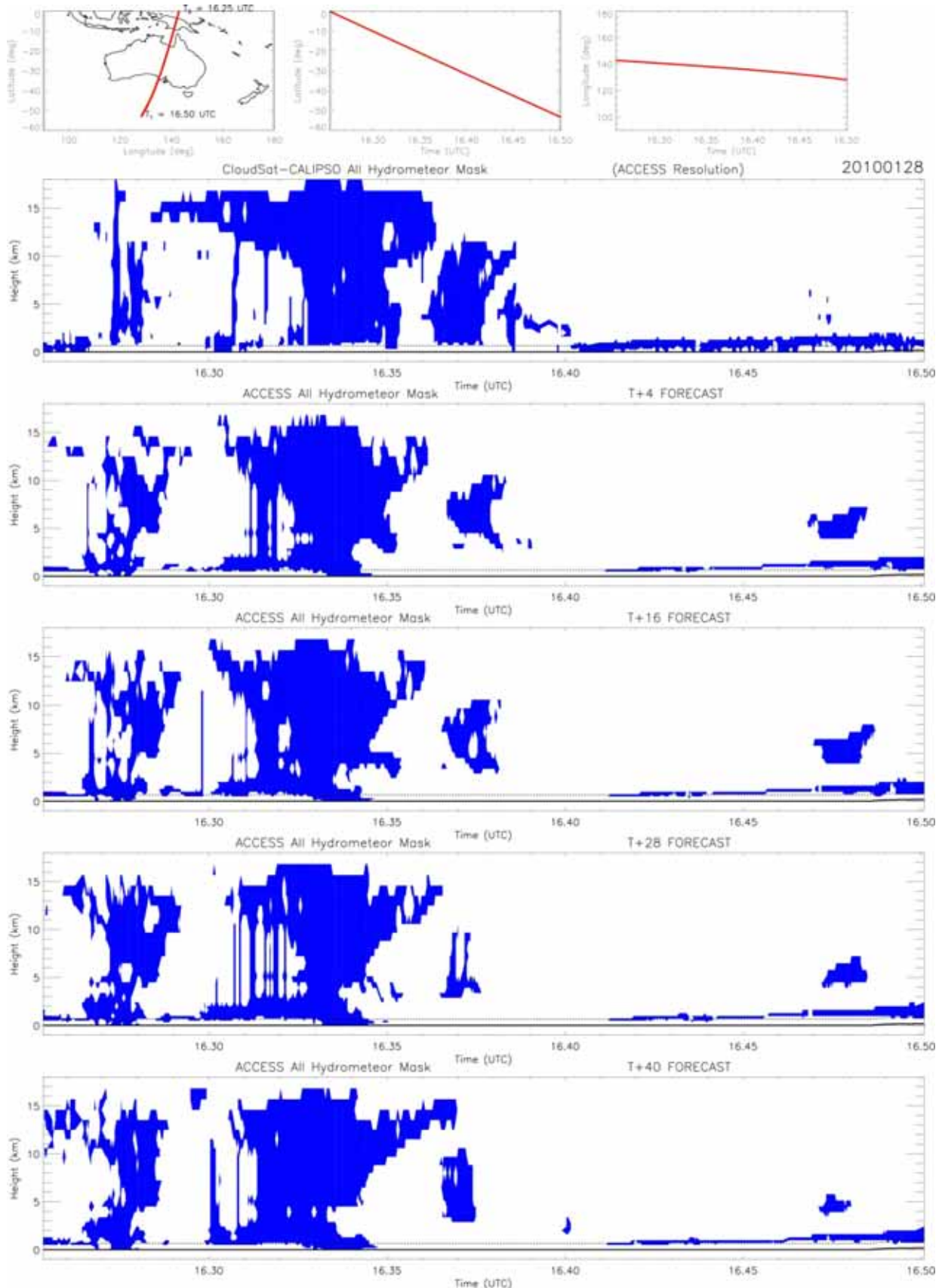


Fig. 2 (a) CloudSat-CALIPSO “model-equivalent” hydrometeor mask, and ACCESS-A simulations for different forecast times : (b) T+4h, (c) T+16h, (d), T+28h, and (e) T+40h.

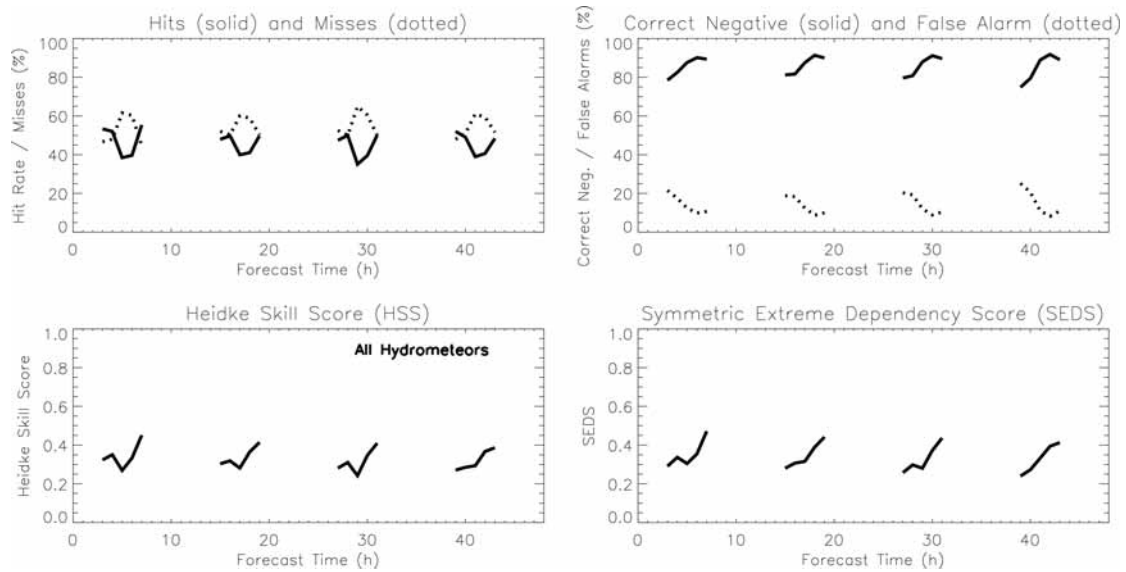


Fig. 3 Skill scores as a function of forecast lead time for 28/01/2010 in the ACCESS-A domain: (a) Hit rate (solid) or misses (dotted), (b) correct negative (solid) or false alarm rate (dotted), (c) HSS, and (d) SEDS (see text).

In order to prepare a further statistical evaluation of clouds and convection produced by the ACCESS system, skill scores have been calculated. The simplest skill scores can be derived from the terms of the contingency table C, which is defined as

$$C = \begin{matrix} \text{Observed} \\ \text{Yes} & \text{No} \\ \begin{pmatrix} a & b \\ c & d \end{pmatrix} & \begin{matrix} \text{Yes} \\ \text{No} \end{matrix} \\ \text{Simulated} \end{matrix}$$

with $n=a+b+c+d$ the total number of points. Using this definition, we can calculate the Hit Rate ($100 a / (a+c)$), the Misses ($100 c / (a+c)$), the Correct negatives ($100 d / (b+d)$), and the False Alarm Rate ($100 b / (b+d)$).

As discussed recently in Hogan et al. (2009), some properties of skill scores are desirable when evaluating cloud properties, in order to avoid misinterpretation. Basically, the skill scores for clouds should be *equitable* (score should be zero for a random forecast, or if the forecast is always the same), *transpose-symmetric* (same score produced when swapping model and observations), *independent of the frequency of occurrence* (because we are interested in rare events such as strong convective storms), and

linear (in order to be able to compute a forecast half-life). Not a lot of scores typically used in the literature have these properties. Hogan et al. (2009) recommended the use of the following generalized skill scores:

The Heidke Skill Score HSS (Heidke, 1926)

$$HSS = \frac{2(ad - bc)}{(a + c)(c + d) + (a + b)(b + d)} \quad (1)$$

The Symmetric Extreme Dependency Score SEDS (Hogan et al. 2009)

$$SEDS = \frac{\ln\{(a + b)/n\} + \ln\{(a + c)/n\}}{\ln\{a/n\}} \quad (2)$$

These scores can be calculated using all points together, or by binning points as a function of the altitude of the hydrometeors (using large layers such as low, mid, high clouds, or using the full vertical profile), as a function of specific regions or weather regimes or latitude bands, and of course as a function of the forecast lead time to evaluate how the skill scores evolve with forecast time. These skill scores must be used when a larger number of samples is available. But with six to eight orbits a day in the simulation domain, a large number of points is easily collected

(typically 20 000 per day). With the evaluation platform built in this study, it is believed that different versions of the model or the impact of any change in the cloud and convective parameterization schemes can be evaluated at the monthly time scale, or maybe even less depending on the nature of the change made in the model. It is anticipated that this very rapid feedback loop will allow for faster improvements of NWP models. The potential of these scores is illustrated in Fig. 3 using all the orbits on 28/01/2010 in the ACCESS-A domain and corresponding model simulations co-located with CloudSat-CALIPSO observations. From this figure it appears that for this particular day the ACCESS-A system predicted 40 to 50 percent of the hydrometeors observed, nearly independent of forecast lead times (Fig. 3a), while it correctly detected the absence of hydrometeors 80 to 90 percent of the time (Fig. 3b). The HSS and SEDS skill scores are ranging from 0.3 to 0.4, which is similar to the values estimated in Hogan et al. (2009) for several European NWP models (including the Met Office Unified Model with 12 km resolution, which is nearly identical to ACCESS-A). It is striking to see that the skill scores show little or no dependency on forecast lead time. This result, if confirmed when more days of comparison are available, could indicate that improvements brought to the representation of clouds should impact all lead times, which is typically not the case of other atmospheric parameters. Obviously these numbers are only indicative and need to be derived from a much larger number of cases, as discussed previously.

Verification of AMV height attribution

The near real-time mask from CALIPSO-CloudSat can also be used for verification of some satellite products before they are assimilated in models, or for improvement of these products. An example of this application follows. Data from the Japanese geostationary satellite MTSAT-1R (and at times MTSAT-2) are received at the Bureau of Meteorology (BoM) and the navigated sequential radiances are used to calculate high density Atmospheric Motion Vectors (AMVs; Le Marshall et al. 2008). These AMVs are generated continuously using infrared (11 μm), visible (0.5 μm) and water vapour absorption (6.7 μm) band images. These AMV data are important for operational numerical

weather prediction (NWP), and particularly for severe weather forecasting, including tropical cyclone track forecasting. In recent assimilation studies using ACCESS, AMVs from MTSAT-1R have been used with 4D-VAR assimilation schemes and their beneficial impact has been demonstrated. A long-term problem associated with the generation of these AMVs has been the height assignment of the wind vectors. The technique employed at BoM for upper-level AMVs is based on the so-called H₂O-intercept method (Schmetz et al. 1993) in which the cloud top altitude is derived from the infrared and water vapor channels. The low-level AMVs altitude assignment technique is that of Le Marshall et al. (2000), where cloud altitude is assigned to the cloud base.

Until now the accuracy of height assignment had been inferred from comparisons with radiosonde measurements. This method has proved useful to some extent and was the only one available so far, but is indirect and sometimes ambiguous. The very different sampling volume of the satellite and the radiosonde measurements is also problematic. The collection of CloudSat-CALIPSO near real-time hydrometeor masks allows for a direct comparison of the cloud height and cloud base assigned in the AMV generation process, and with similar horizontal resolution. As in the case of the model cloud evaluation, so far only case studies have been looked at. A database is presently being built in order to test further the existing height assignment methods statistically and ultimately to improve these height assignment techniques.

Conclusions

In the present paper we describe a platform for the evaluation of clouds and convection generated by the regional and limited-area versions of the operational Australian NWP system (ACCESS) using near real-time products of the CloudSat and CALIPSO mission. The use of this platform for the verification of assimilated satellite products is also highlighted. A case study is given to illustrate the great potential for model verification and parameterization improvement. This platform will now be integrated as part of the operational process, in order to collect a large statistical sample and monitor skill scores for the ACCESS system.

Acknowledgements

The NASA CloudSat CPR data and products were obtained from the CloudSat Data Processing Center run by the Cooperative Institute for Research in the Atmosphere (CIARA). The CALIPSO expedited data were obtained from the NASA Langley Research Center Atmospheric Science Data Center.

References

- Bony, S. and co-authors. 2006. How Well Do We Understand and Evaluate Climate Change Feedback Processes? *J. Climate*, **19**, 3445–82.
- Comstock, J.M., Ackerman, T.P. and Mace, G.G. 2002. Ground-based lidar and radar remote sensing of tropical cirrus clouds at Nauru Island: Cloud statistics and radiative impacts. *J. Geophys. Res.*, **107** (D23), 4714, doi:10.1029/2002JD002203.
- Delanoë, J. and Hogan, R.J. 2008. A variational scheme for retrieving ice cloud properties from combined radar, lidar and infrared radiometer. *J. Geophys. Res.*, **113**, D07204, doi:10.1029/2007JD009000.
- Donovan, D.P. and van Lammeren, A.C.A.P. 2001. Cloud effective particle size and water content profile retrievals using combined lidar and radar observations -I. Theory and examples. *J. Geophys. Res.*, **106**, 27425-48.
- Dufresne, J.-L. and Bony, S. 2008. An assessment of the primary sources of spread of global warming estimates from coupled atmosphere-ocean models. *J. Climate*, **21**, 5135–44.
- Heidke, P. 1926. Calculation of the success and goodness of strong wind forecasts in the storm warning service. *Geogr. Ann. Stockholm*, **8**: 301–49.
- Hogan, R.J., O'Connor, E. and Illingworth, A. 2009. Verification of cloud-fraction forecasts. *Q. J. R. Meteorol. Soc.* **135**: 1494–1511.
- Illingworth, A.J. and co-authors. 2007. CLOUDNET – Continuous evaluation of cloud profiles in seven operational models using ground-based observations. *Bull. Amer. Meteor. Soc.*, **88**, 883-98.
- Jakob, C. 2002. Ice clouds in numerical weather prediction models: Progress, problems and prospects, in Cirrus, edited by D. Lynch et al. pp. 327–345, Oxford Univ. Press, New York.
- Le Marshall, J.F., Seecamp, R., Dunn, M., Velden, C., Wanzong, S., Puri, K., Bowen, R. and Rea, A. 2008. The contribution of locally-generated MTSAT-1R atmospheric motion vectors to operational meteorology in the Australian region. *Aust. Met. Mag.*, **57**, 359-65.
- Le Marshall, J.F., Pescod, N., Seecamp, R., Rea, A., Tingwell, C., Ellis, G. and Shi, H. 2000. Recent Advances in the quantitative generation and assimilation of high spatial and temporal resolution satellite winds. *Proc. Fifth International Winds Workshop*, Lorne, Australia, 28-31 March 2000. Published by EUMETSAT EUM P28 ISSN 1023-0414. 47-56.
- Mace, G.G. and co-authors. 2009. A description of hydrometeor layer occurrence statistics derived from the first year of merged Cloudsat and CALIPSO data. *J. Geophys. Res.*, **114**, D00A26, doi:10.1029/2007JD009755.
- Mitrescu, C., Miller, S., Hawkins, G., L'Ecuyer, T., Turk, J., Partain, P. and Stephens, G. 2008. Near real time applications of CloudSat data, *J. Appl. Meteorol.*, **47**, 1982–1994.
- Protat, A. and co-authors 2009. Assessment of CloudSat reflectivity measurements and ice cloud properties using ground-based and airborne cloud radar observations. *J. Atmos. Oceanic Technol.*, **26** (9), 1717-41.
- Protat, A., Armstrong, A., Haeffelin, M., Morille, Y., Pelon, J., Delanoë, J. and Bouniol, D. 2006: Impact of conditional sampling and instrumental limitations on the statistics of cloud properties derived from cloud radar and lidar at SIRTa. *Geophys. Res. Letters*, **33**, L11805, doi:10.1029/2005GL025340.
- Sassen, K. and Cho, B.S. 1992: Subvisual-Thin Cirrus Lidar Dataset for Satellite Verification and Climatological Research. *J. Appl. Meteor.*, **31**, 1275–85.
- Schmetz, J., Holmlund, K., Hoffman, J., Strauss, B., Mason, B., Gaertner, V., Koch, A. and Van Der Berg, L. 1993. Operational cloud motion winds from METEOSAT infrared images. *J. Appl. Meteor.*, **32**, 1206-55.
- Stephens, G. L. and co-authors. 2002. The CloudSat mission and the A-train: A new dimension of space-based observations of clouds and precipitation. *Bull. Amer. Meteor. Soc.*, **83**, 1771–90.
- Tinel, C., Testud, J., Pelon, J., Hogan, R.J., Protat, A., Delanoë, J. and Bouniol, D. 2005. The retrieval of ice-cloud properties from cloud radar and lidar synergy. *J. Appl. Meteor.*, **44**, 860–75.
- Vaughan, M. A. et al. 2009. Fully Automated Detection of Cloud and Aerosol Layers in the CALIPSO Lidar Measurements, *J. Atmos. Oceanic Technol.*, **26**, 2034–50.
- Winker, D. M. et al. 2009. Overview of the CALIPSO Mission and CALIOP Data Processing Algorithms, *J. Atmos. Oceanic Technol.*, **26**, pp. 2310-23.